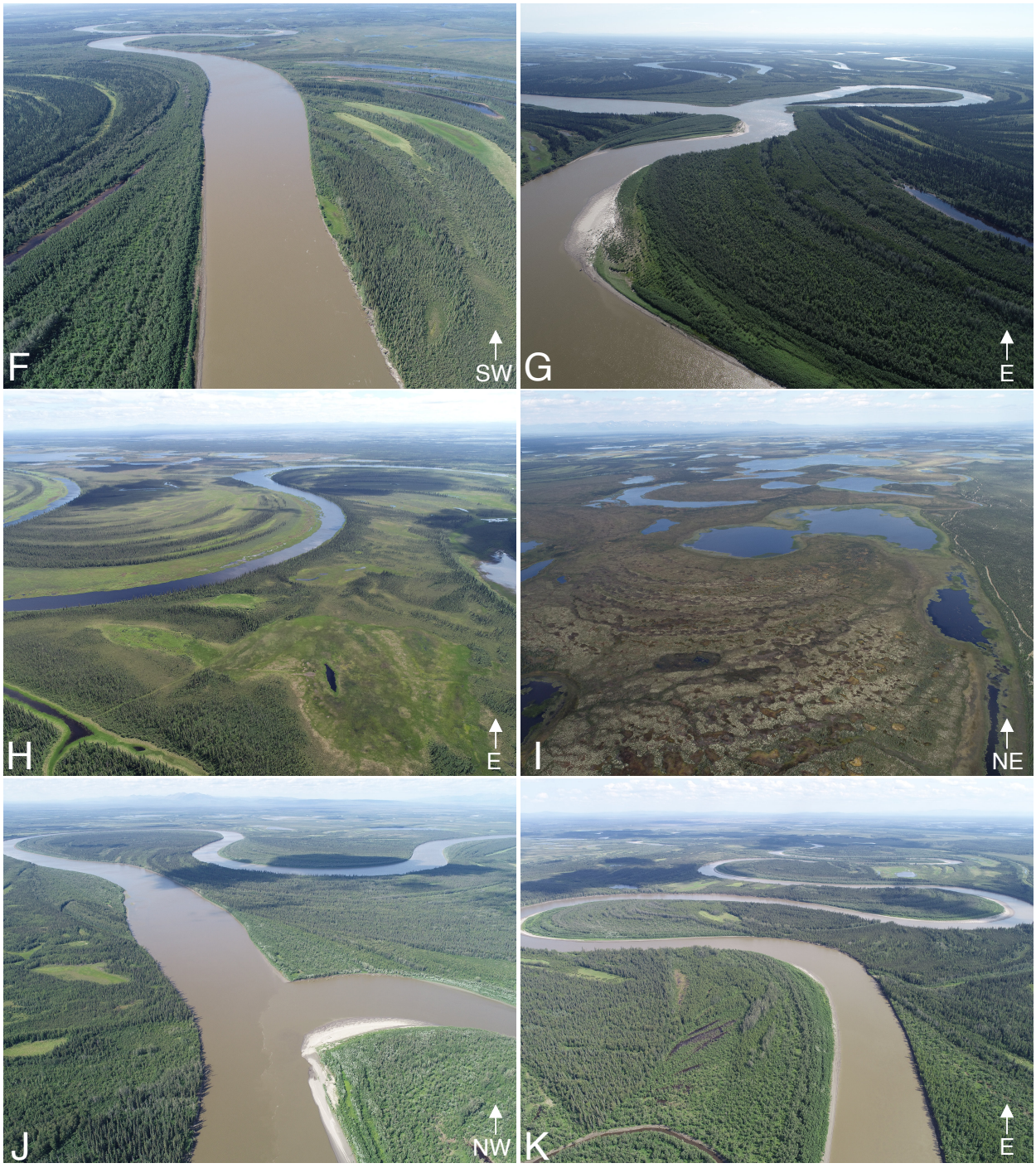

Fig. S1 (*continued*): (F) Linear stretch of the Koyukuk River where multiple suspended sediment depth profiles were collected. (G) River cutoff, with oxbow lakes in the background. (H) Former meanders. (I) Multiple lakes east of Huslia. (J) Northern fork of the upstream confluence. (K) Eastern fork of the upstream confluence.

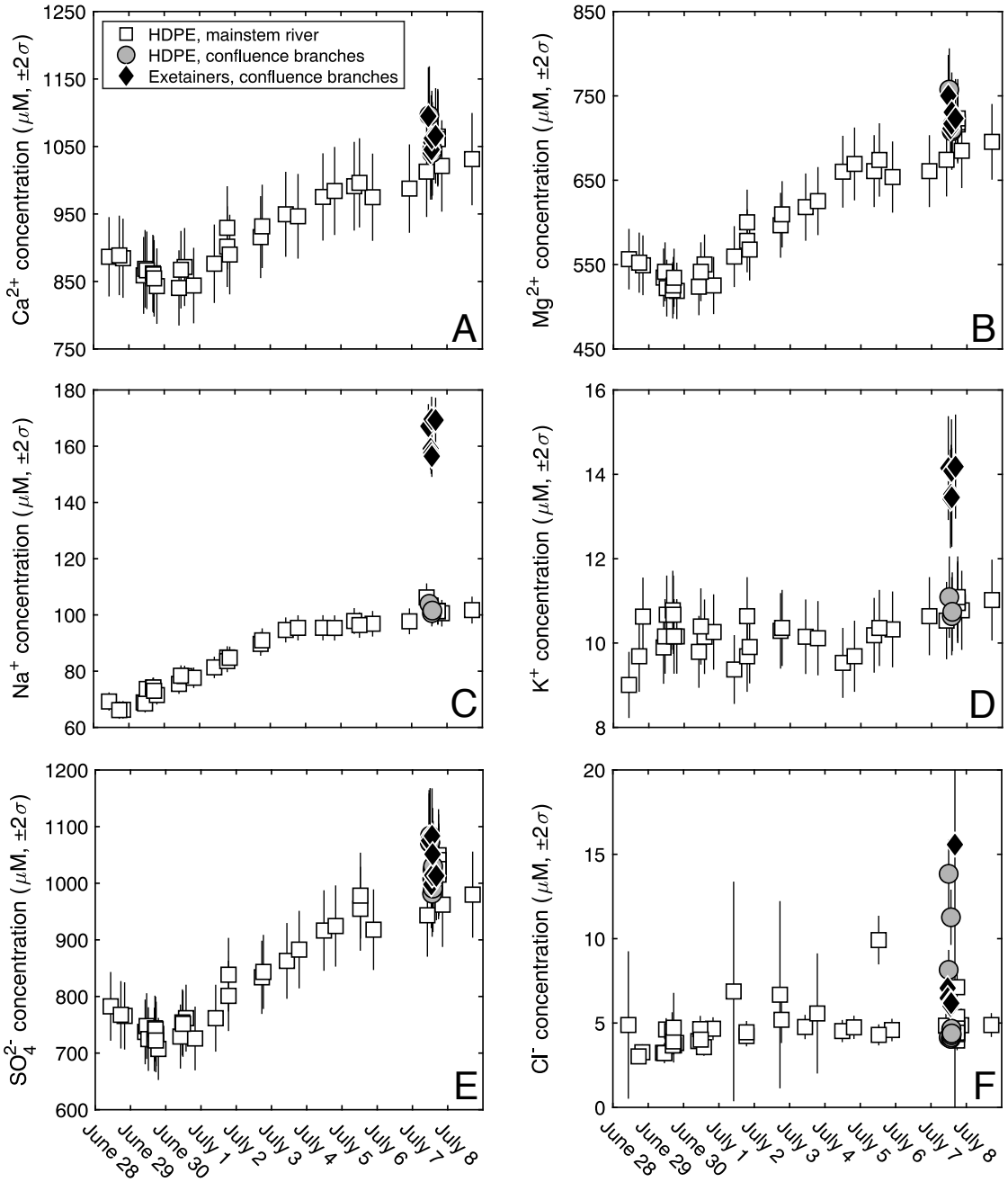

Fig. S2: Major ion concentrations of Koyukuk River samples coded by sample location and collection bottle for (A) Ca^{2+}, (B) Mg^{2+}, (C) Na^{+}, (D) K^{+}, (E) SO_4^{2-}, and (F) Cl^{-}. While most mainstem samples were collected near Huslia, several samples were also collected from a confluence north of Huslia (Figs. S1J, S1K). Samples from upstream of the confluence were collected into both exetainer vials (black diamonds) and HDPE (grey circles) and compared to mainstem samples collected downstream of the confluence into HDPE (white squares). Samples collected into exetainer vials had large deviations from both the expected trends and from the same water collected into HDPE. These data suggest the existence of a chemical blank on the exetainers and we excluded all samples collected into exetainers from the analysis. To be as conservative as possible, we also excluded data collected in HDPE bottles from upstream of the confluence so all sample represent a single-threaded reach of Koyukuk River.

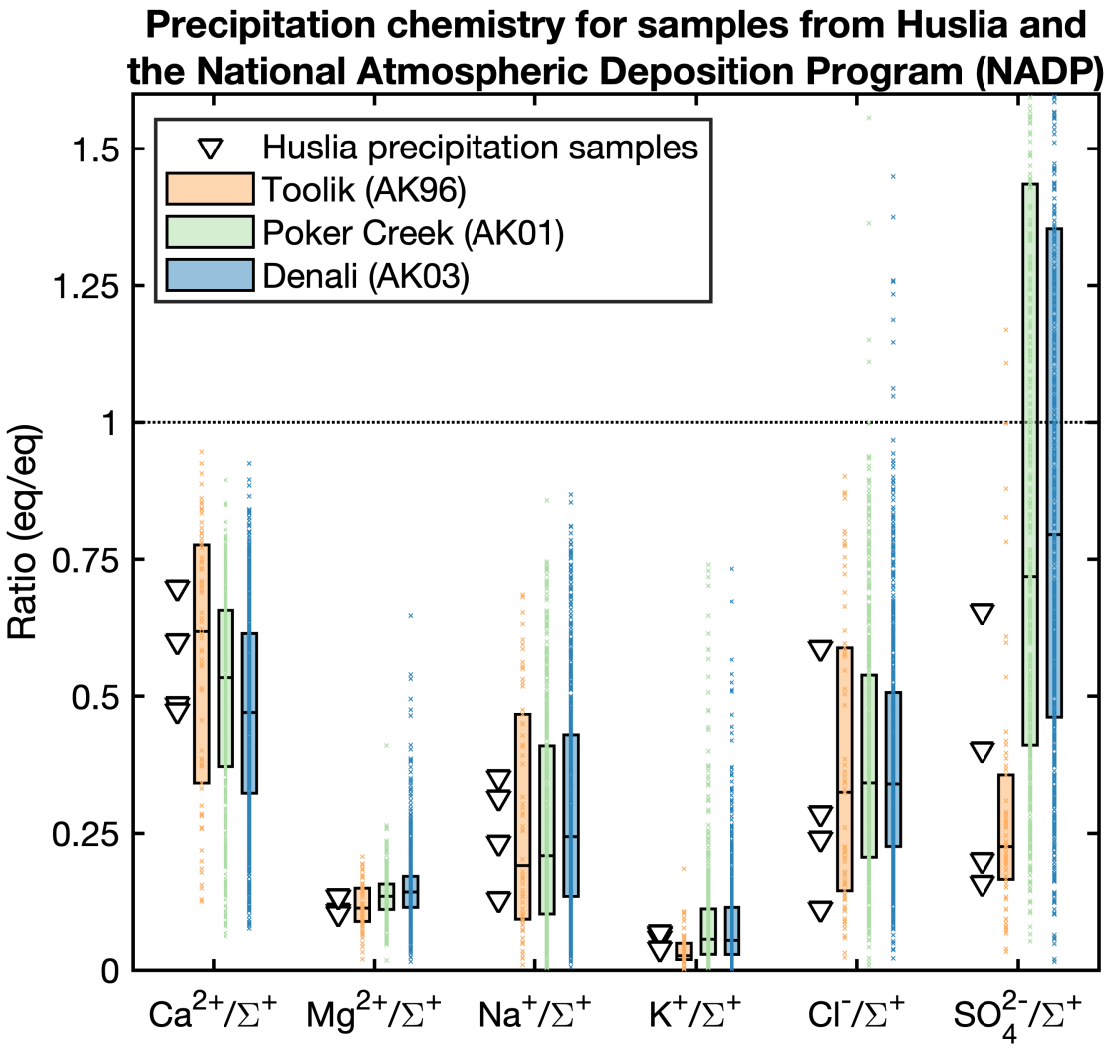

Fig. S3: Major ion ratios of the four new precipitation samples collected near Huslia compared to samples from Toolik (AK96, orange), Poker Creek (AK01, green) and Denali (AK03, blue) measured as part of the National Atmospheric Deposition Program (NADP). Plotted symbols are individual observations, shaded regions span from the 25th to 75th percentiles of observations, and horizontal black bars indicating median values.

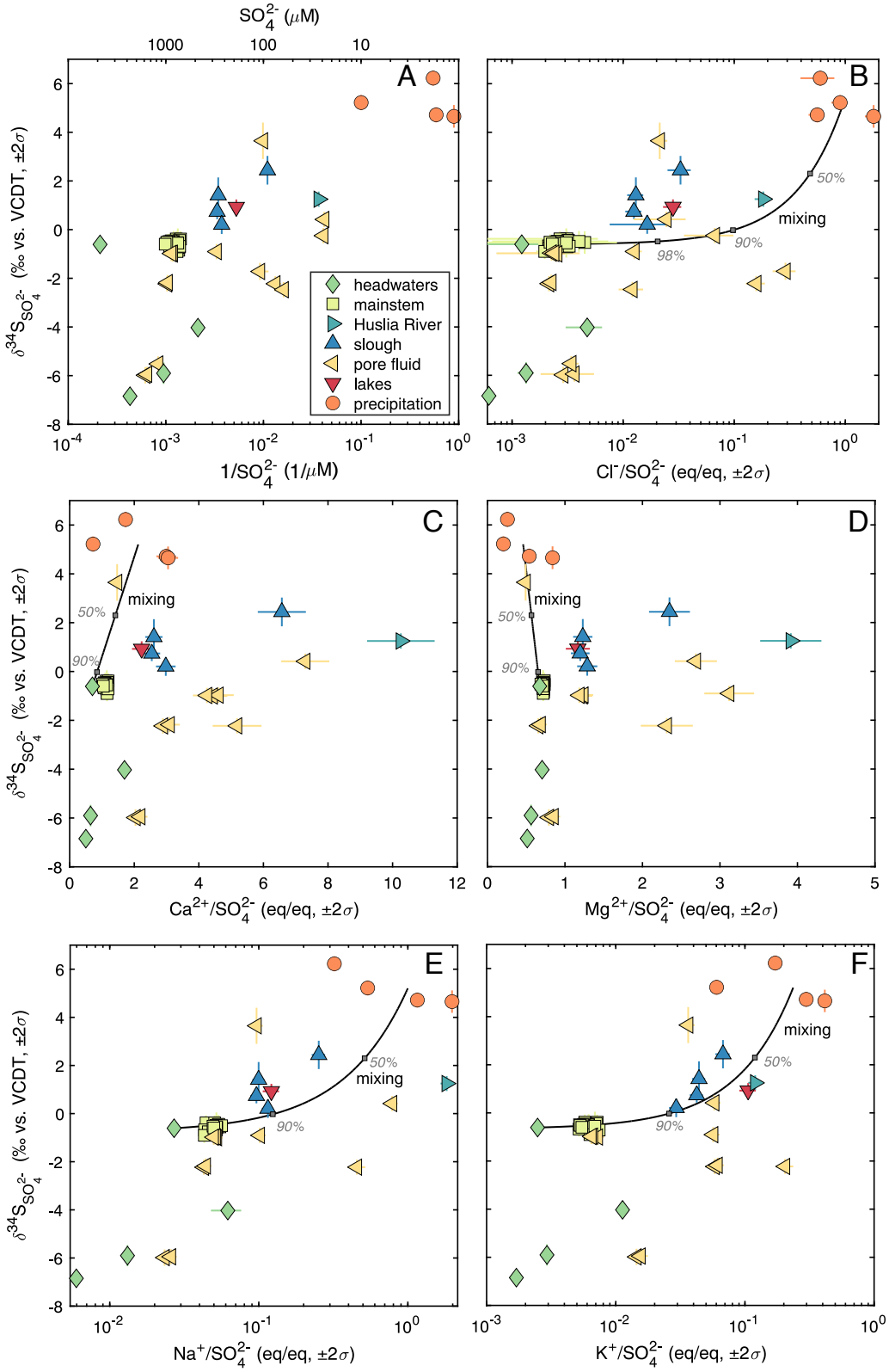

Fig. S4: Sulfur isotope mixing diagrams. $\delta^{34}S_{SO4}$ against (A) $1/SO_4^{2-}$, (B) Cl^-/SO_4^{2-}, (C) Ca^{2+}/SO_4^{2-}, (D) Mg^{2+}/SO_4^{2-}, (E) Na^+/SO_4^{2-}, and (F) K^+/SO_4^{2-}. The major ion chemistry is consistent with a combination of mixing, microbial sulfate reduction, and the addition of cations from weathering.

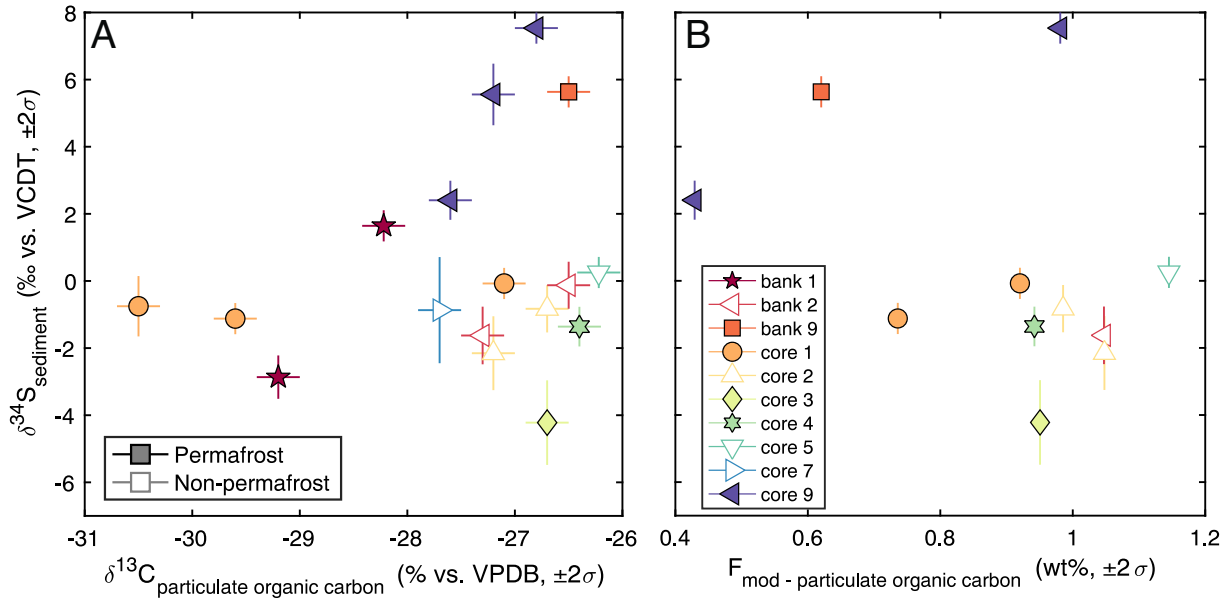

Fig. S5: Sedimentary sulfur and carbon isotope ratios. $\delta^{34}S_{sediment}$ against (A) $\delta^{13}C_{particulate\ organic\ carbon}$ and (B) $F_{mod\text{-}particulate\ organic\ carbon}$ (Douglas et al., 2022). There are not clear relationships between $\delta^{34}S_{sediment}$ and either the $\delta^{13}C$ or F_{mod} values of POC, or with whether samples are from permafrost (closed symbols) or non-permafrost (open symbols) deposits.

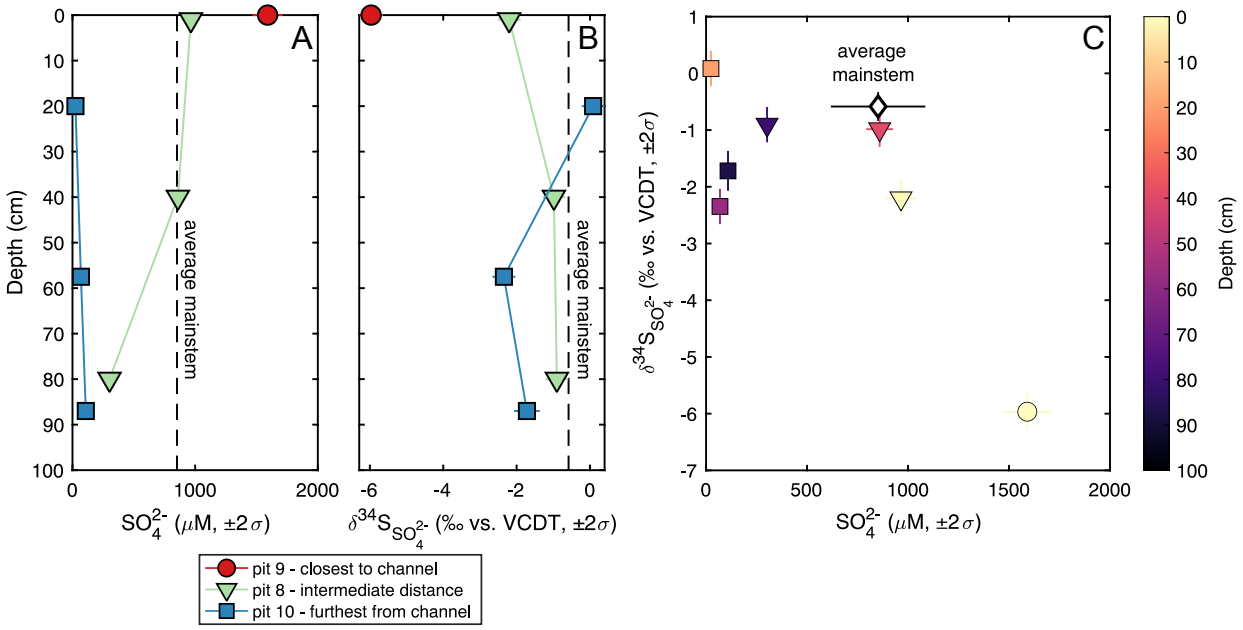

Fig. S6: Pore fluid (A) SO_4^{2-} concentration and (B) $\delta^{34}S_{SO4}$ values against sampling depth for a transect orthogonal to the active channel. Samples were collected at multiple time points from three neighboring sites: next to the active channel (pit 9), at an intermediate distance (pit 8), and furthest away (pit 10). (C) Cross plots of $\delta^{34}S_{SO4}$ and SO_4^{2-} concentration shape-coded by sample location and color-coded by depth of sample collection. The lowest $\delta^{34}S_{SO4}$ values are found close to the channel and have high SO_4^{2-} concentrations, while the highest $\delta^{34}S_{SO4}$ value is found furthest from the channel with low SO_4^{2-} concentration.

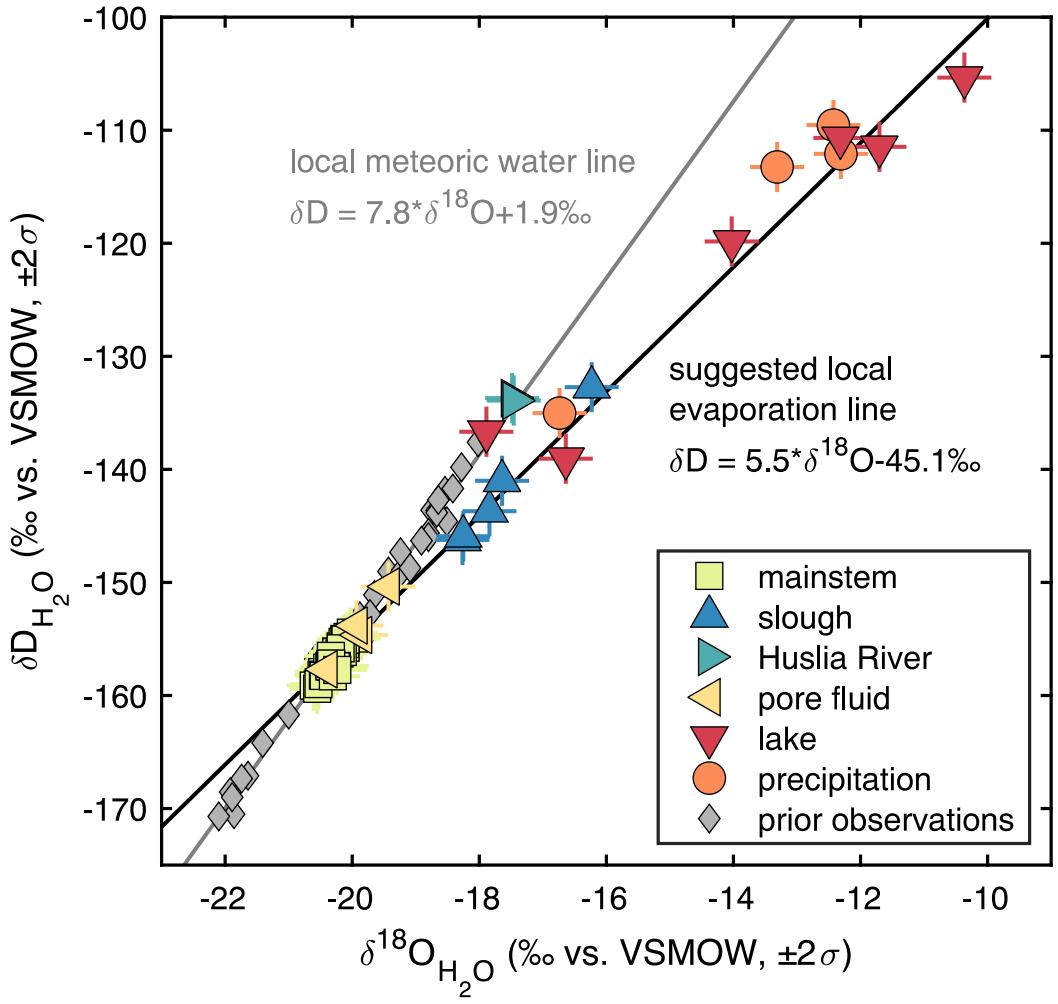

Fig. S7: Measurements of $\delta^{18}O_{H2O}$ and δD_{H2O} in samples from the Koyukuk River catchment and prior observations. The mainstem river and pore fluid samples agree with the local meteoric water line, as defined by prior observations, while lake and slough samples are largely consistent with a local evaporation line.

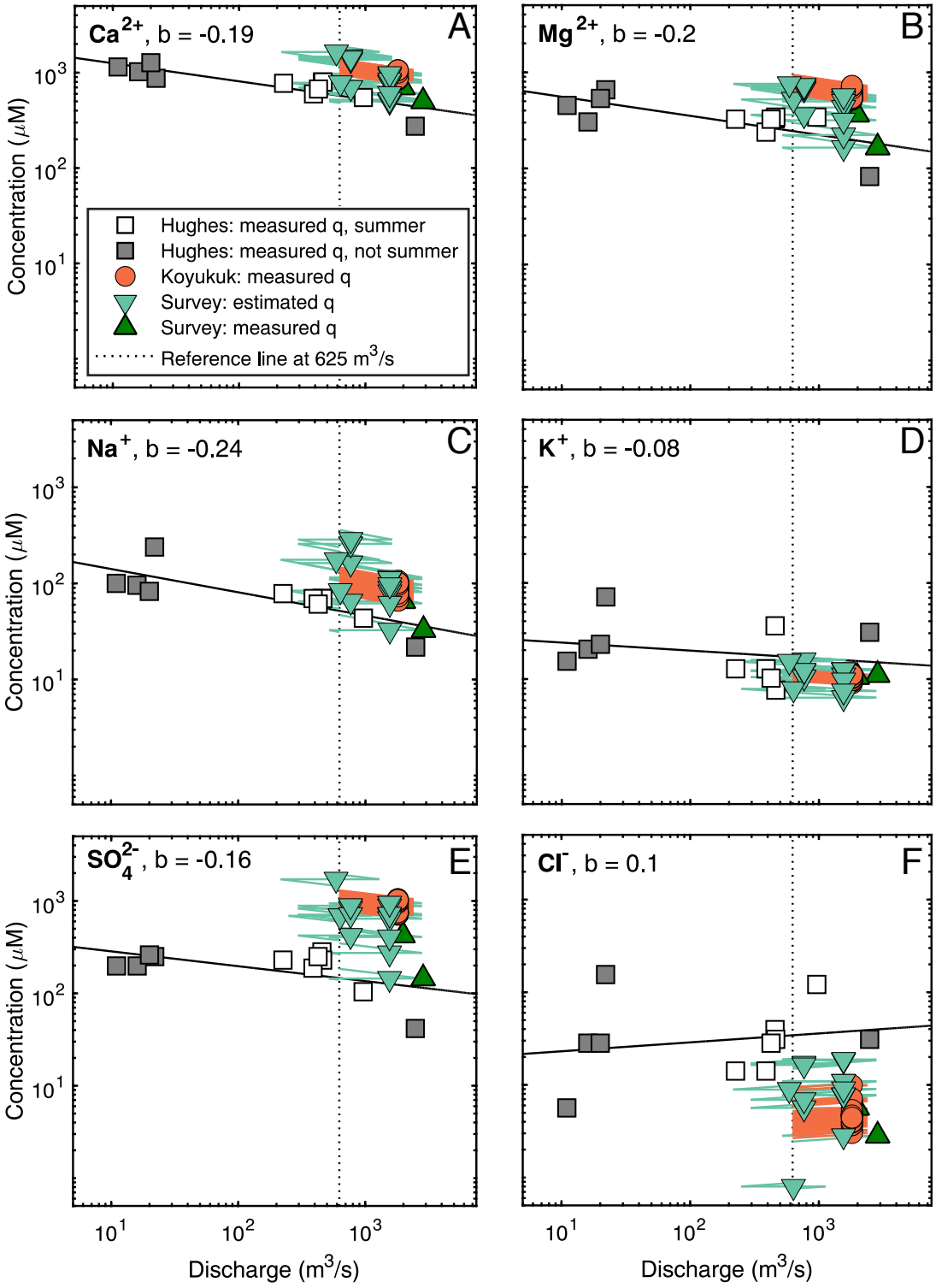

Fig. S8: Concentration and discharge for (A) Ca^{2+}, (B) Mg^{2+}, (C) Na^{+}, (D) K^{+}, (E) SO_4^{2-} and (F) Cl^{-}. Observations are plotted for Hughes summer months (June-September, white squares), Hughes non-summer months (grey squares), 2018 samples collected near Huslia (orange circles), and for additional observations from the Koyukuk River catchment (light and dark green triangles). Concentrations were scaled to 625 m^3/s using the calculated b values and either observed or estimated discharge, with error bars reflecting the range of considered discharge values.

Appendix S3: Additional inversion results

Table S2: The mean of median end-members fractional contribution to river dissolved load in scenario 1 (without CO_2 degassing), scenario 2 (CO_2 degassing < 2.5x measured DIC, results reported in the main text) and scenario 3 (CO_2 degassing < 25x measured DIC) for all mainstem and slough samples together and independently. Note that the sum of median contributions does not necessarily equal 100% even while the sum of fractional contributions for each element was between 95% and 105% for each simulation in the inversion.

Variable	End-member	All samples			Mainstem			Slough		
		Scenario: 1	2	3	1	2	3	1	2	3
DIC	Carbonate	68.5%	72.7%	72.2%	70.9%	75.6%	75%	52.8%	53.5%	53.9%
	C_{org} oxidation	31.5%	38.5%	37.5%	29.1%	36.6%	35.6%	47.3%	50.7%	49.7%
	Degassing	-	-10.7%	-9.1%	-	-11.7%	-10.1%	-	-3.9%	-2.6%
Ca^{2+}	Carbonate	69%	75.2%	75.5%	66.5%	73.4%	73.7%	85.2%	86.7%	87%
	Evaporite	15.8%	15.7%	15.5%	17%	16.9%	16.6%	8.1%	8.1%	8.3%
	Silicate	10.3%	4.6%	4.1%	11.2%	5%	4.5%	1.9%	1.9%	1.9%
	Precipitation	0.5%	0.5%	0.5%	0.5%	0.5%	0.5%	1%	1%	1%
Mg^{2+}	Carbonate	67.4%	70.4%	69.5%	64.3%	67.6%	66.5%	87.6%	88.6%	89.2%
	Silicate	32.4%	29.4%	30.3%	35.6%	32.2%	33.4%	11.9%	10.9%	10.3%
	Precipitation	0.2%	0.2%	0.2%	0.2%	0.2%	0.2%	0.5%	0.5%	0.5%
Na^{+}	Silicate	94.2%	94.2%	94.2%	95.2%	95.2%	95.1%	88%	88%	88.2%
	Precipitation	5.8%	5.8%	5.8%	4.8%	4.8%	4.9%	12%	12%	11.8%
K^{+}	Silicate	90.8%	90.6%	90.8%	90.8%	90.5%	90.7%	91.5%	91.6%	91.6%
	Precipitation	9.2%	9.4%	9.2%	9.2%	9.5%	9.3%	8.5%	8.4%	8.4%
Cl^{-}	Precipitation	100%	100%	100%	100%	100%	100%	100%	100%	100%
SO_4^{2-}	H_2SO_4 production	79.4%	79.6%	79.7%	80.7%	80.7%	81%	71.2%	71.9%	70.7%
	Evaporite	20%	19.8%	19.8%	19%	18.9%	18.6%	26.5%	25.7%	27.2%
	Precipitation	0.6%	0.6%	0.6%	0.3%	0.3%	0.3%	2.2%	2.2%	2.1%

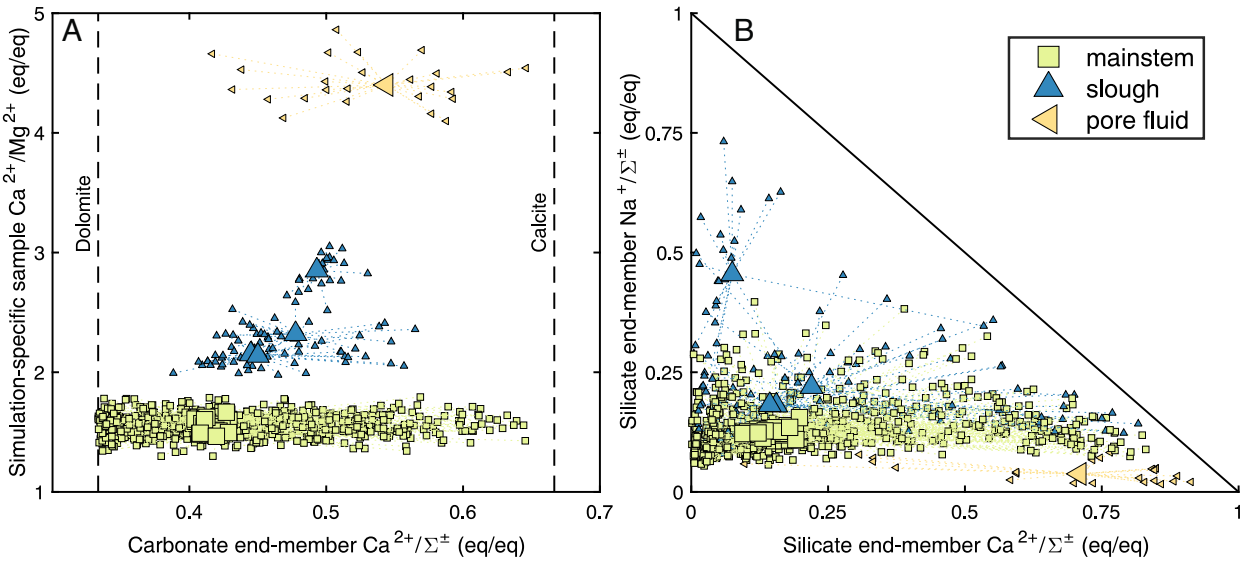

Fig. S9: Inversion-constrained end-member chemistry. Large symbols reflect median sample results, which are connected by dotted lines to small symbols reflecting 25 successful individual simulation results for each sample. (A) Simulation-specific sample Ca^{2+}/Mg^{2+} against $Ca^{2+}/\Sigma^{\pm}$ in the carbonate end-member. MEANDIR constrained the carbonate end-member to have lower $Ca^{2+}/\Sigma^{\pm}$ in mainstem samples than in slough samples or pore fluids. The reduced $Ca^{2+}/\Sigma^{\pm}$ values in mainstem samples likely indicates weathering of dolomite, and very few results were found where the carbonate end-member resembled calcite. The inversion constrained the $Ca^{2+}/\Sigma^{\pm}$ of carbonate weathering in the slough samples at intermediate values; this indicates that the slough samples have insufficient dissolved Ca^{2+} and Mg^{2+}, relative to the carbonate contribution required by their relative DIC abundance and $\delta^{13}C_{DIC}$ observations, for the carbonate end-member to be either pure calcite or dolomite. (B) Inversion-constrained silicate $Na^{+}/\Sigma^{\pm}$ against silicate $Ca^{2+}/\Sigma^{\pm}$. The silicate end-member was unconstrained during inversion and attained lower $Na^{+}/\Sigma^{\pm}$ ratios in mainstem samples than in the slough samples. Silicate $Na^{+}/\Sigma^{\pm}$ and $K^{+}/\Sigma^{\pm}$ were well correlated across all samples but with distinct slopes.

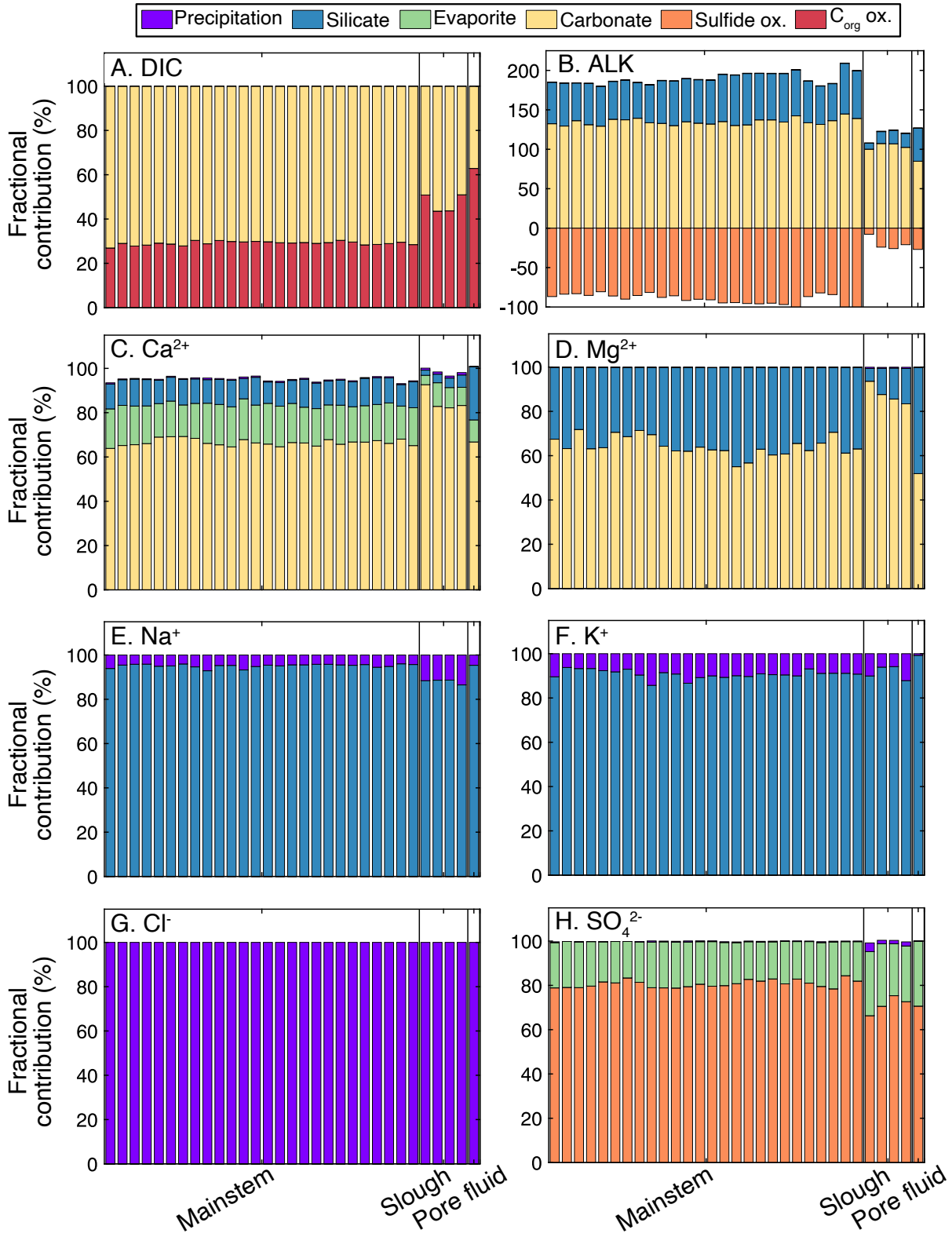

Fig. S10: Median end-member contributions for scenario 1, where degassing is not included in the inversion. Fractional contributions of the precipitation, silicate, evaporite, carbonate, sulfide oxidation, and C_{org} oxidation end-members to (A) DIC, (B) ALK, (C) Ca^{2+}, (D) Mg^{2+}, (E) Na^{+}, (F) K^{+}, (G) Cl^{-}, and (H) SO_4^{2-}. Note that the sum of median contributions does not need to equal 100%.

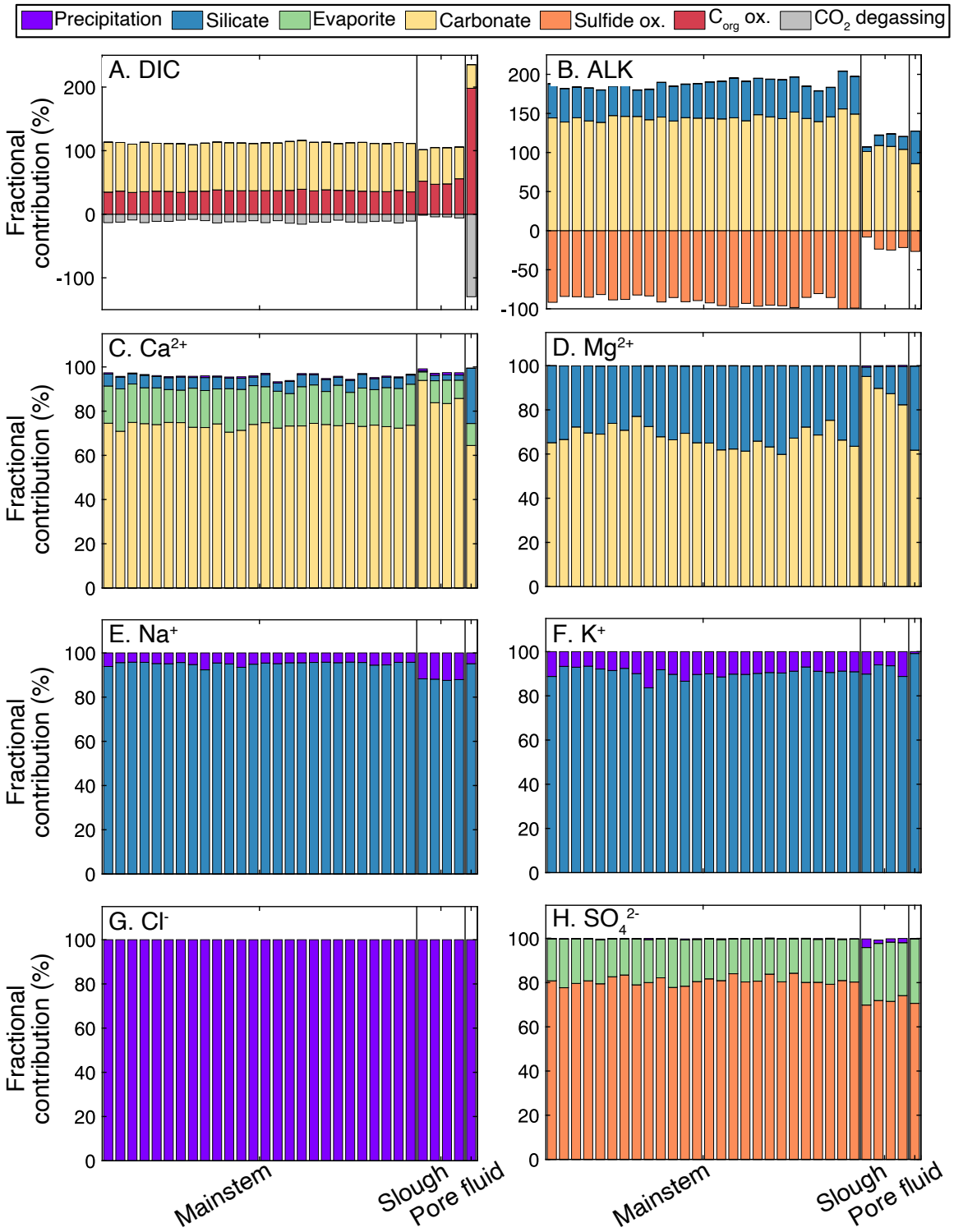

Fig. S11: Median end-member contributions for scenario 2, where degassing is constrained to < 2.5x DIC and the degassing fractionation factor is between -10.1‰ and -7.6‰. Fractional contributions of the precipitation, silicate, evaporite, carbonate, sulfide oxidation, C_{org} oxidation, and CO_2 degassing end-members to (A) DIC, (B) ALK, (C) Ca^{2+}, (D) Mg^{2+}, (E) Na^{+}, (F) K^{+}, (G) Cl^{-}, and (H) SO_4^{2-}. Note that the sum of DIC sourced from carbonate weathering and C_{org} oxidation can exceed 100% because the fractional contribution of CO_2 degassing to DIC is negative.

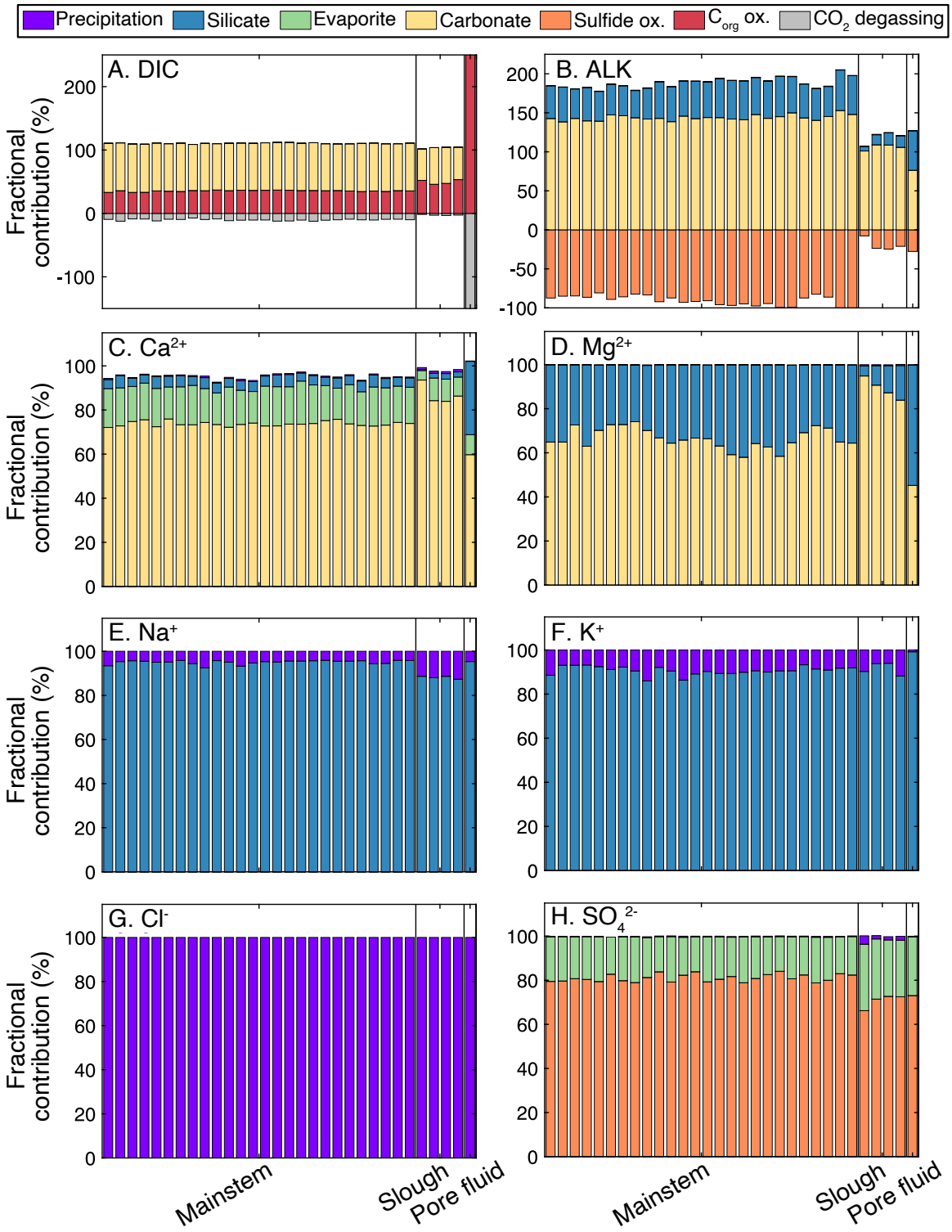

Fig. S12: Median end-member contributions for scenario 3, where degassing is constrained to < 25x DIC and the degassing fractionation factor is between -10.1‰ and -7.6‰. Fractional contributions of the precipitation, silicate, evaporite, carbonate, sulfide oxidation, C_{org} oxidation, and CO_2 degassing end-members to (A) DIC, (B) ALK, (C) Ca^{2+}, (D) Mg^{2+}, (E) Na^{+}, (F) K^{+}, (G) Cl^{-}, and (H) SO_4^{2-}. Note that the sum of DIC sourced from carbonate weathering and C_{org} oxidation can exceed 100% because the fractional contribution of CO_2 degassing to DIC is negative.

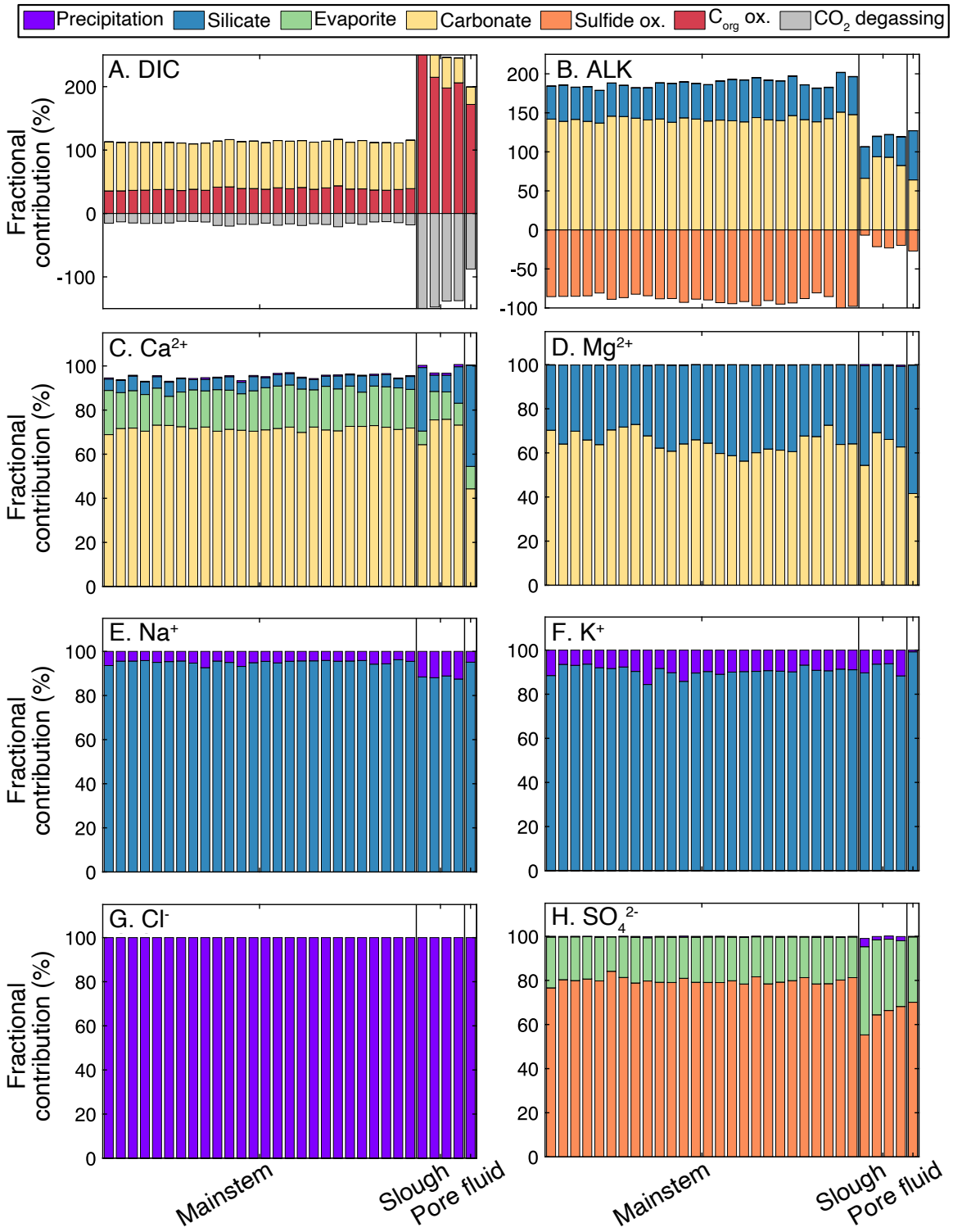

Fig. S13: Median end-member contributions for scenario 4, where degassing is constrained to < 2.5x DIC and the degassing fractionation factor is between -20‰ and 0‰. Fractional contributions of the precipitation, silicate, evaporite, carbonate, sulfide oxidation, C_{org} oxidation, and CO_2 degassing end-members to (A) DIC, (B) ALK, (C) Ca^{2+}, (D) Mg^{2+}, (E) Na^{+}, (F) K^{+}, (G) Cl^{-}, and (H) SO_4^{2-}. Note that the sum of DIC sourced from carbonate weathering and C_{org} oxidation can exceed 100% because the fractional contribution of CO_2 degassing to DIC is negative.

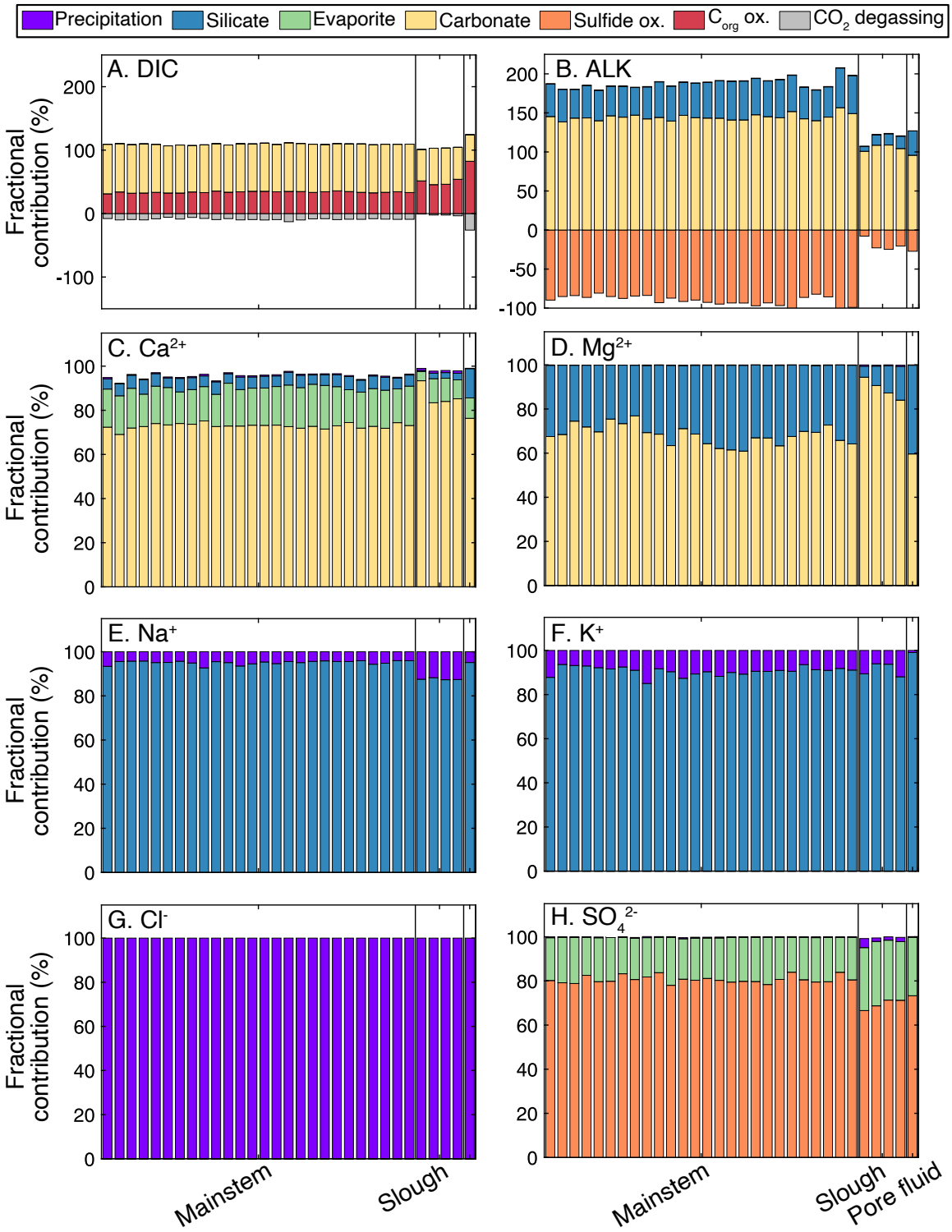

Fig. S14: Median end-member contributions for scenario 5, where degassing is constrained to < 2.5x DIC and the degassing fractionation factor is between -10.1‰ and 0‰. Fractional contributions of the precipitation, silicate, evaporite, carbonate, sulfide oxidation, C_{org} oxidation, and CO_2 degassing end-members to (A) DIC, (B) ALK, (C) Ca^{2+}, (D) Mg^{2+}, (E) Na^{+}, (F) K^{+}, (G) Cl^{-}, and (H) SO_4^{2-}. Note that the sum of DIC sourced from carbonate weathering and C_{org} oxidation can exceed 100% because the fractional contribution of CO_2 degassing to DIC is negative.

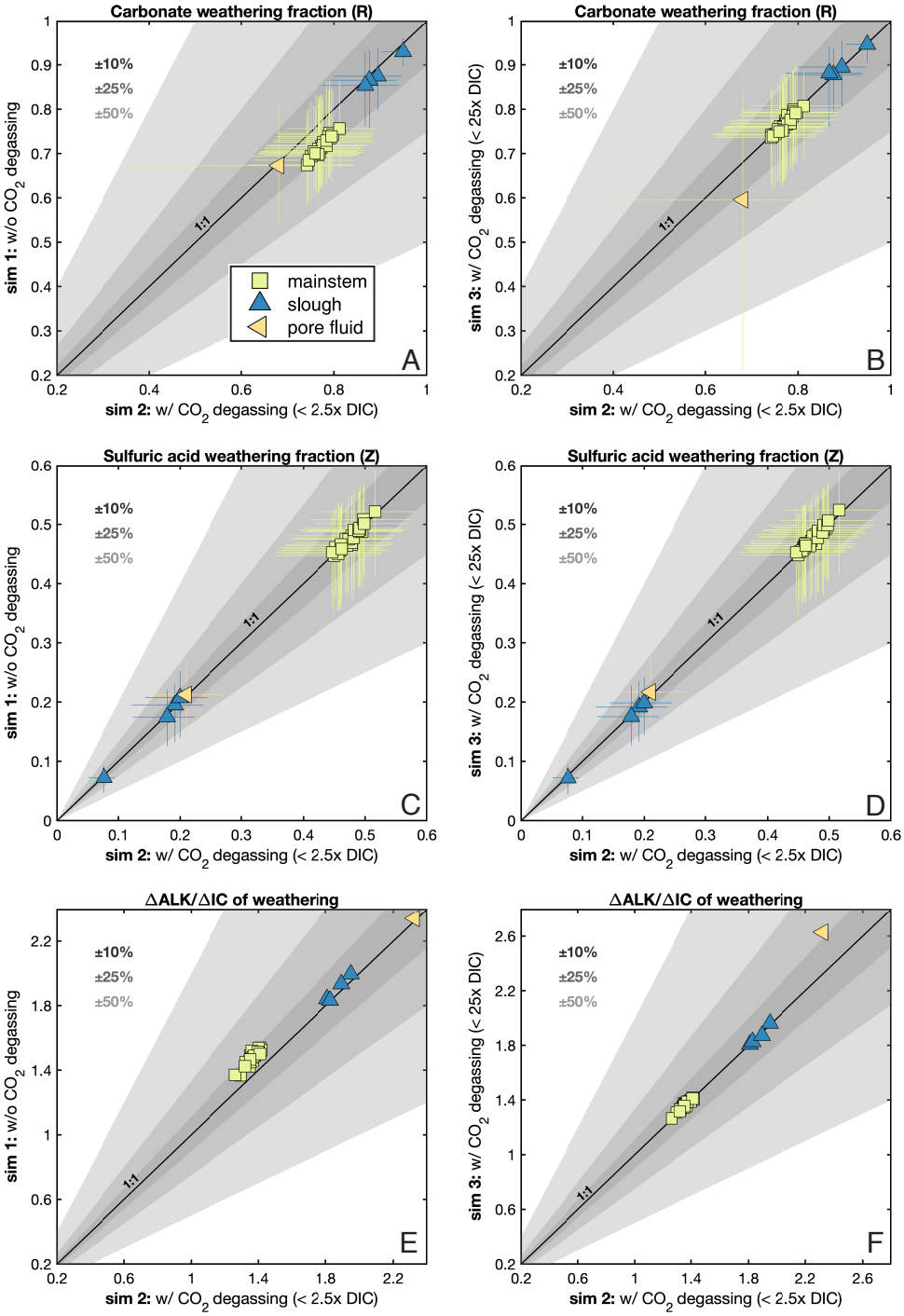

Fig. S15: Sensitivity of MEANDIR inversion results to inclusion of degassing. Median inversion results without degassing (simulation 1) and results with <25x DIC degassing (simulation 3) are plotted against inversion results with <2.5x DIC degassing (simulation 2, used in the main text) for (A, B) the fraction of weathering alkalinity sourced from carbonate (R), (C, D) the fraction of weathering alkalinity offset through sulfide oxidation (Z), and (E, F) the median ΔALK/ΔIC of chemical weathering calculated from R and Z. All panels include 1:1 lines, dark grey shading indicates ±10%, medium shading indicates ±25%, and light grey shading indicates ±50%. In (A)-(D), error bars range from 5th to 95th percentiles of inversion results.

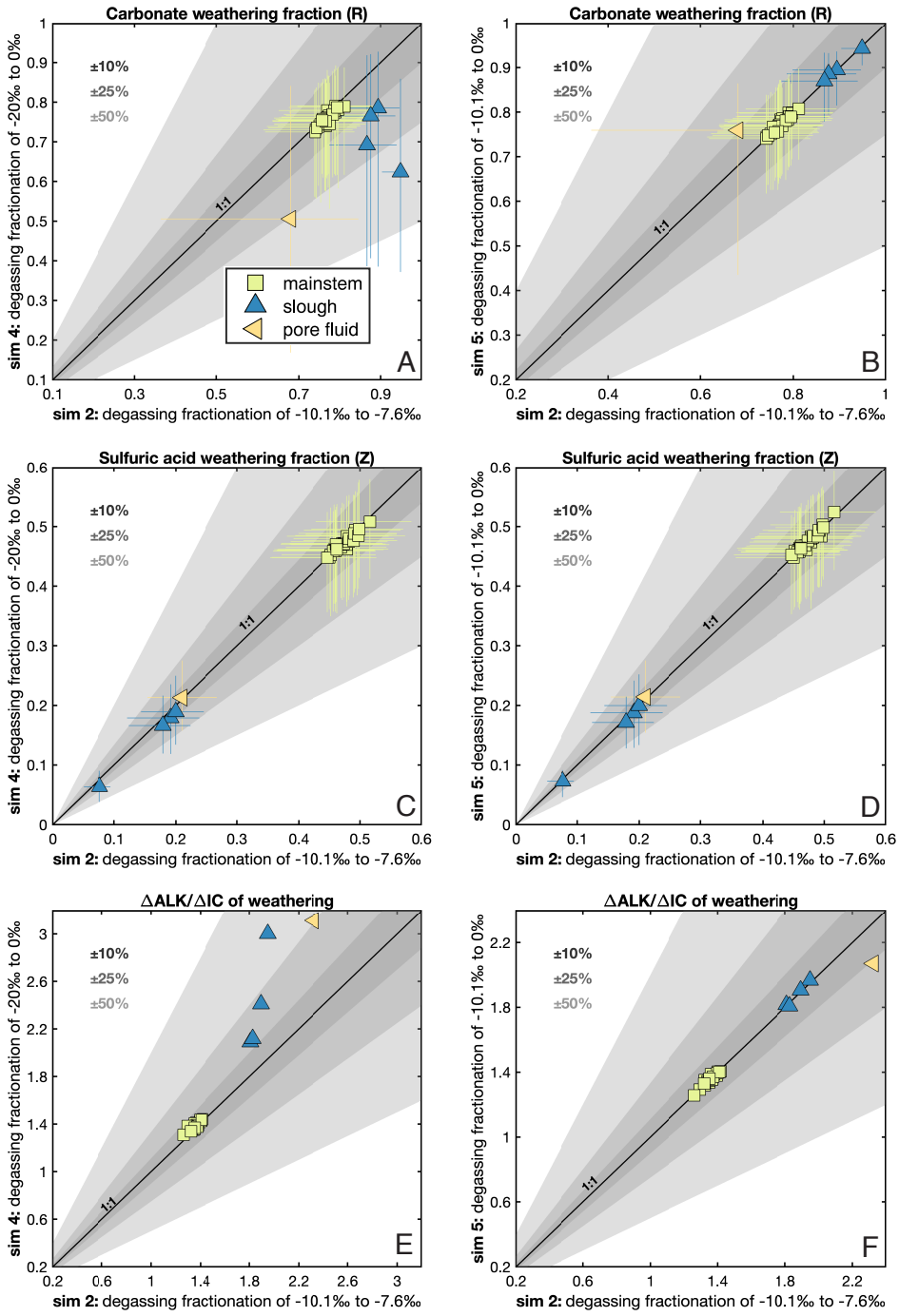

Fig. S16: Sensitivity of MEANDIR inversion results to inclusion of degassing. Median inversion results with the degassing fractionation factor between -20‰ and 0‰ (simulation 4) and between -10.1‰ and 0‰ (simulation 5) are plotted against inversion results with the degassing fractionation factor between -10.1‰ and -7.6‰ (simulation 2, used in the main text) for (A, B) the fraction of weathering alkalinity sourced from carbonate (R), (C, D) the fraction of weathering alkalinity offset through sulfide oxidation (Z), and (E, F) the median ΔALK/ΔIC of chemical weathering calculated from R and Z. All panels include 1:1 lines, dark grey shading indicates ±10%, medium shading indicates ±25%, and light grey shading indicates ±50%. In (A)-(D), error bars range from 5th to 95th percentiles of inversion results.

Appendix S4: Review of selected prior fluvial observations in the Yukon River Basin

Prior studies of Alaskan rivers flowing through permafrost landscapes have identified both seasonal and decadal trends in river water chemistry attributed to seasonal active layer thaw, decadal active layer deepening, and the shifting contributions of shallow and deep flow paths (Table S3). Studies of inorganic solute seasonality have focused on the region surrounding the Toolik Field Station (Keller et al., 2007, 2010; Barker et al., 2014; Lehn et al., 2017), the Caribou-Poker Creek Research Watershed (CPCRW; MacLean et al., 1999; Petrone et al., 2006, 2007), and the Chena River (Douglas et al., 2013), while longer-term observations have been made on the Yukon River at Pilot Station (Toohey et al., 2016). Here we review several studies to highlight patterns in the relationship between seasonal hydrology and weathering that provide additional context for interpreting the measurements in the Koyukuk River reported in the main text.

The chemical weathering reactions expressed along different flow paths reflect mineral availability, reactant supply, and reaction kinetics. As a simple example, although even minor abundances of highly reactive phases can dominate river dissolved load (Blum et al., 1998; White et al., 1999), a weathering system could not oxidize pyrite to sulfuric acid or dissolve carbonate if these phases were absent (West et al., 2005). Weathering reactions also require the delivery of oxidants and acids, as well as the removal of reaction products. Furthermore, the residence time of water in the subsurface regulates the time available for weathering to occur (Maher and Chamberlain, 2014; Maher and Druhan, 2014). Shallow flow paths with short residence times have little time for water-rock interaction and favor chemical weathering reactions with rapid kinetics, such as carbonate weathering and sulfide oxidation, while deeper flow paths with longer residence times are associated with silicate weathering reactions (Tipper et al., 2006).

Keller et al. (2007) identified depletion of carbonate in the top ~1 m of sites near Toolik Lake, with older sites showing a greater extent of carbonate removal from the active layer relative to the underlying permafrost. These observations motivated the prediction that deepening of the active layer over multiple years might result in enhanced carbonate weathering as thaw reached previously frozen carbonate-rich sediment. If such increases in carbonate weathering exceeded increases in silicate weathering due to longer flow paths, then active layer deepening would result in an increased fraction of carbonate weathering in the total weathering budget. Indeed, Keller et al. (2010) later identified increasing Ca^{2+}/Na^{+} and decreasing $^{87}Sr/^{86}Sr$ ratios in the nearby Toolik Lake inlet stream between 1994 and 2004 for samples collected at low discharge during July and August. Overall, these studies identified vertical structure in the availability of carbonate and a decadal trend towards higher relative carbonate weathering fraction during the low-discharge late-summer period.

Lehn et al. (2017) reported additional sediment chemistry and seasonal river observations for five catchments near Toolik Lake. The river samples were collected in 2009 and 2010 between the freshet and freeze-up and included three mountainous catchments, the Atigun, Roche Moutonnee, and the Trevor, as well as two tundra sites, the Upper Kuparuk and the Imnavait. The mountainous sites had elevated precipitation-corrected $(Ca^{2+}+Mg^{2+})/Na^{+}$ ratios during the spring freshet relative to early summer, which Lehn et al. (2017) attributed to a pulse of water characterized by high carbonate weathering fraction followed by increases in the fraction of silicate weathering due to expression of water from deeper flow paths. Data from the Upper Kuparuk showed a similar trend, while that from Imnavait Creek were more consistent with a summer transition towards elevated carbonate weathering fraction. In the late summer, Lehn et al. (2017) invoked dissolution of sulfate salts to explain increases in precipitation-corrected

(Ca^{2+}+Mg^{2+})/Na^{+} and SO_4^{2-}/(Ca^{2+}+Mg^{2+}) ratios at the mountain sites (Wadham et al., 2001; Cooper et al., 2002; Gooseff et al., 2002; Lopez et al., 2007; Rutter et al., 2011). This interpretation relied on the argument that SO_4^{2-}/(Ca^{2+}+Mg^{2+}) ratios exceeded 0.5, which was assumed to be the maximum SO_4^{2-}/(Ca^{2+}+Mg^{2+}) ratio attainable for sulfuric acid weathering of carbonate. However, the 0.5 value reflects only one possible weathering reaction, and the SO_4^{2-}/(Ca^{2+}+Mg^{2+}) ratio can attain nearly arbitrary positive values during weathering (Kemeny and Torres, 2021). Late-summer weathering of sulfate salts is a possible, but non-unique, interpretation of the Toolik Lake data.

As an alternative explanation of the Lehn et al. (2017) observations, measurements from the mountain watersheds are also consistent with increasing summertime sulfide oxidation coupled with a source of either Ca^{2+} or Mg^{2+}. These late summer changes could reflect increases in the fraction of shallow flow paths or seasonal thaw of the active layer into sediment rich in carbonate and sulfur-bearing phases (Keller et al., 2007; 2010). Moreover, the salt-based and sulfide-based interpretations of the data are not mutually exclusive if the seasonal salts form through evaporative concentration of weathering-derived solutes. That is, if the SO_4^{2-} and Ca^{2+} or Mg^{2+} in sulfate salts are ultimately derived from sulfuric acid and carbonate weathering products, wintertime storage as $CaSO_4$ and $MgSO_4$ merely represents a delay in the release of weathering ions rather than a fundamentally different type of weathering. The situation is further complicated by consideration of whether seasonal salts weather early during the freshet (Cooper et al., 2002) or towards the end of the summer (Lehn et al., 2017).

Outside of the Toolik Field Station, MacLean et al. (1999) and Petrone et al. (2006) reported observations of fluvial chemistry from a high-permafrost catchment and a neighboring low-permafrost catchment in the CPCRW near Fairbanks. These studies revealed that the high-permafrost river waters displayed lower volume-weighted concentration of Mg^{2+} and lower ratios

of Ca^{2+}/Na^{+} than the low-permafrost catchment (Fig. S17A, B). Discharge and Ca^{2+}/Na^{+} were positively related in all catchments. Unlike the studies discussed below, the CPCRW data did not support a clear relationship between SO_4^{2-}/Σ^{+} and discharge (Fig. S17E). We interpret these observations as evidence for a greater proportion of solutes derived from carbonate weathering at higher discharge, consistent with the framework of Tipper et al. (2006).

In the Chena River near Fairbanks, Douglas et al. (2013) found that dissolved $^{87}Sr/^{86}Sr$ ratios were positively related to discharge but negatively related to Ca^{2+}/Sr^{2+} ratios (Fig. S18). These authors proposed that the radiogenic high-discharge flows reflected silicate weathering near the surface due to depletion of carbonate and that non-radiogenic low-discharge flows reflected carbonate weathering at depth. The $^{87}Sr/^{86}Sr$ ratios were also negatively related to Na^{+}/Σ^{+} and Si/Σ^{+} but positively related to Ca^{2+}/Na^{+}. We speculate whether or not the radiogenic signal at high discharge might actually reflect weathering of a carbonate lithology with high $^{87}Sr/^{86}Sr$ and low Ca^{2+}/Sr^{2+} ratios rather than a silicate end-member. As in the Himalaya, carbonates with variable Ca^{2+}/Sr^{2+} and variable but elevated $^{87}Sr/^{86}Sr$ ratios have been identified throughout the Yukon River Basin (Edmond, 1992; Keller et al., 2007; Bataille et al., 2014; Brennan et al., 2014; Lehn et al., 2017; Kang et al., 2022). Under this interpretation, the Chena River expressed heightened carbonate weathering fractions during the spring and summer and a larger fraction of silicate weathering during fall flow.

Toohey et al. (2016) identified increases in the annual fluxes of Ca^{2+}, Mg^{2+}, Na^{+}, and SO_4^{2-} within the Yukon River between 1982 and 2014. For the most part, the annually-integrated relative abundances of Ca^{2+}, Mg^{2+}, Na^{+}, and SO_4^{2-} have not changed by more than a few percent (Fig. S19). During this thirty-year period the molar Ca^{2+}/Na^{+} ratio declined from about 7 to about 6.5, Ca^{2+}/Σ^{+} declined from ~70% to ~67%, Mg^{2+}/Σ^{+} increased from ~25.5% to ~28%, Na^{+}/Σ^{+} was variable but

largely unchanged, and SO_4^{2-}/Σ^+ increased from ~21% to ~27%. These trends can be interpreted in several ways and their effect on atmospheric pCO_2 depends on the origins of the increasing Ca^{2+}, Mg^{2+}, and SO_4^{2-}. Toohey et al. (2016) attributed the increasing SO_4^{2-} flux to either dissolution of a calcium sulfate salt or sulfide oxidation; the former would only indirectly impact the carbon cycle (Shields and Mills, 2021) while the latter would increase pCO_2 on timescales less than ~10 Myr (Torres et al., 2014). The sulfur and oxygen isotopic ratios of SO_4^{2-} could distinguish between these two SO_4^{2-} sources and measuring these ratios in river water collected at Pilot Station is a natural next step in interpreting evidence for increases in fluvial SO_4^{2-} and SO_4^{2-}/Σ^+.

In synthesis, the base flow of rivers running through permafrost landscapes might typically be dominated by deep flows with long residence times and products of silicate weathering reactions. The seasonal freshet then rapidly increases the fraction of channel water sourced from shallow flow paths, causing river chemistry to reflect products of rapid chemical weathering reactions if and when relevant minerals are available. The fraction of summer water sourced from shallow flow paths is expected to fall below the freshet fraction while exceeding the winter fraction and reflect an intermediate degree of carbonate and silicate weathering. The ratio of carbonate and silicate weathering products can vary with the hydrograph and effects of integrated warming over the course of the summer. Increases in the fraction of carbonate weathering products could result from increases in the fraction of shallow flow relative to deep flow (Tipper et al., 2006) or from seasonal thaw of the active layer into carbonate-rich sediment (Keller et al., 2007). Conversely, summertime increases in silicate weathering could occur as discharge declines to base flow values or if seasonal changes in active layer thickness lengthen the mean residence time of expressed flow paths. The formation and dissolution of salts over seasonal and annual timescales can impact fluvial chemistry but represents only transient storage of weathering products.

Table S3. Selected prior work on seasonal and annual changes in permafrost river solutes.

Seasonal trends				
Study	**Location**	**Freshet**	**Summer**	**Notes**
Lehn et al. (2017)	Toolik mountain sites	High carbonate weathering	Increased silicate weathering and evaporite dissolution	Sulfate salt dissolution is only necessary if $H_2SO_4 + CaCO_3$ has $SO_4^{2-}/(Ca^{2+}+Mg^{2+}) \leq 0.5$.
Petrone et al. (2006)	CPCRW	N/A	Increased carbonate weathering with increased discharge	Summertime discharge increases for 2/3 catchments, with rising Ca^{2+}/Na^{+}, Ca^{2+}/Σ^{+}
Douglas et al. (2013)	Chena River	High silicate weathering	Increased carbonate weathering with decreasing discharge	Radiogenic carbonate would mean freshet has high carbonate weathering with summertime transition to silicate weathering
Annual trends				
Study	**Location**	**Observations**		**Notes**
Keller et al. (2010)	Toolik Lake inlet	Increasing carbonate weathering during late summer months		Data from July and August, 1994-2004, discharge <1.1 m^3/s
Toohey et al. (2016)	Yukon River	Increasing Ca^{2+}, Mg^{2+}, SO_4^{2-} fluxes with large increase in SO_4^{2-}/Σ^{+}		Enhanced sulfide oxidation or evaporite dissolution

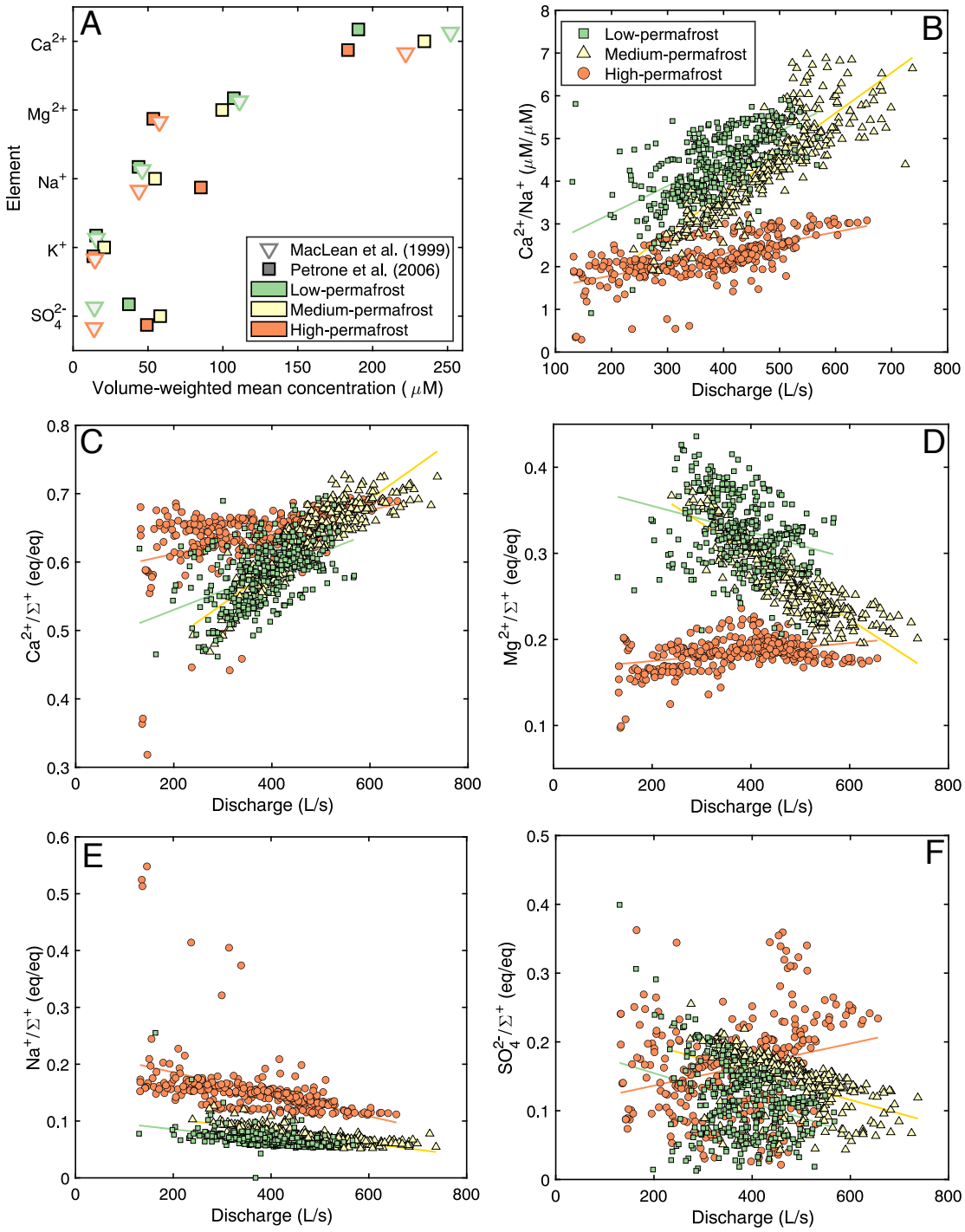

Fig. S17: Prior observations from the Caribou-Poker Creek Research Watershed (CPCRW). (A) Volume-weighted mean concentration of dissolved solutes in low-permafrost, medium-permafrost, and high-permafrost streams (MacLean et al., 1999; Petrone et al., 2006). (B) Ca^{2+}/Na^{+}, (C) Ca^{2+}/Σ^{+}, (D) Mg^{2+}/Σ^{+}, (E) Na^{+}/Σ^{+}, and (F) SO_4^{2-}/Σ^{+} against discharge for samples from the low-permafrost (green squares), medium-permafrost (yellow triangles), and high-permafrost (orange circles) rivers (Petrone et al., 2006). The data suggest that increasing discharge was associated with increased carbonate weathering without coherent changes in the relative abundance of SO_4^{2-}. Data in (B)-(F) were provided directly by Dr. Petrone.

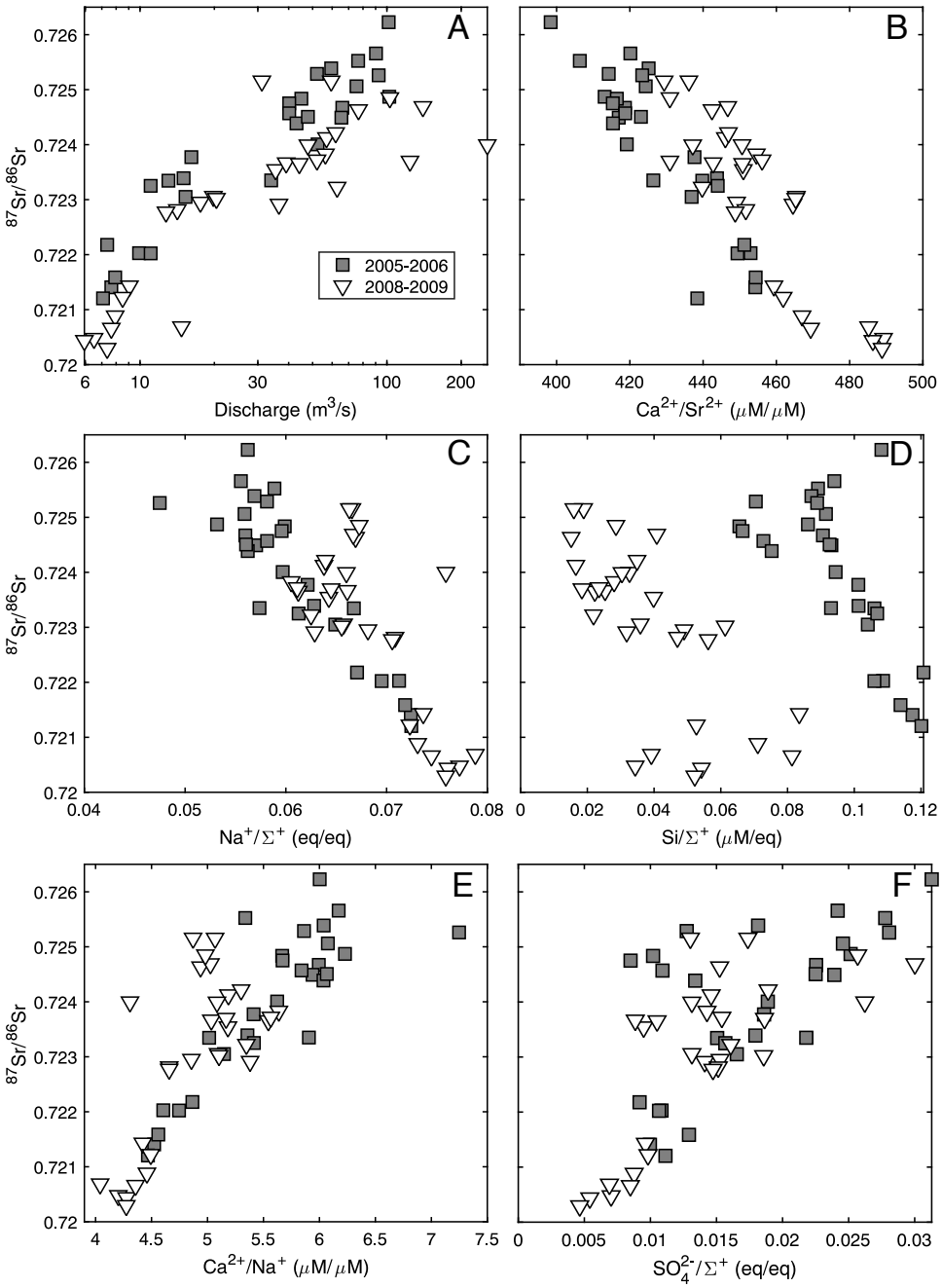

Fig. S18: Prior observations from the Chena River (Douglas et al., 2013). As discussed in the original article, the dissolved $^{87}Sr/^{86}Sr$ ratios were (A) positively related to discharge and (B) negative related to Ca^{2+}/Sr^{2+}. These data were interpreted as showing that higher discharge was associated with weathering of radiogenic silicate minerals and lower discharge with weathering of non-radiogenic carbonate minerals with high Ca^{2+}/Sr^{2+} ratios. However, the $^{87}Sr/^{86}Sr$ ratio was also negatively related to (C) Na^+/Σ^+ and (D) Si/Σ^+ while (E) positively related to Ca^{2+}/Na^+ and (F) SO_4^{2-}/Σ^+. These observations led us to speculate whether higher discharge was actually associated with enhanced carbonate weathering and sulfide oxidation rather than silicate weathering. As in the Himalaya, carbonates with elevated $^{87}Sr/^{86}Sr$ ratios are known to occur within the Yukon River Basin (Edmond, 1992; Bataille et al., 2014; Brennan et al., 2014; Lehn et al., 2017; Kang et al., 2022). Data from Douglas et al. (2013) were reported in their Tables 1-4.

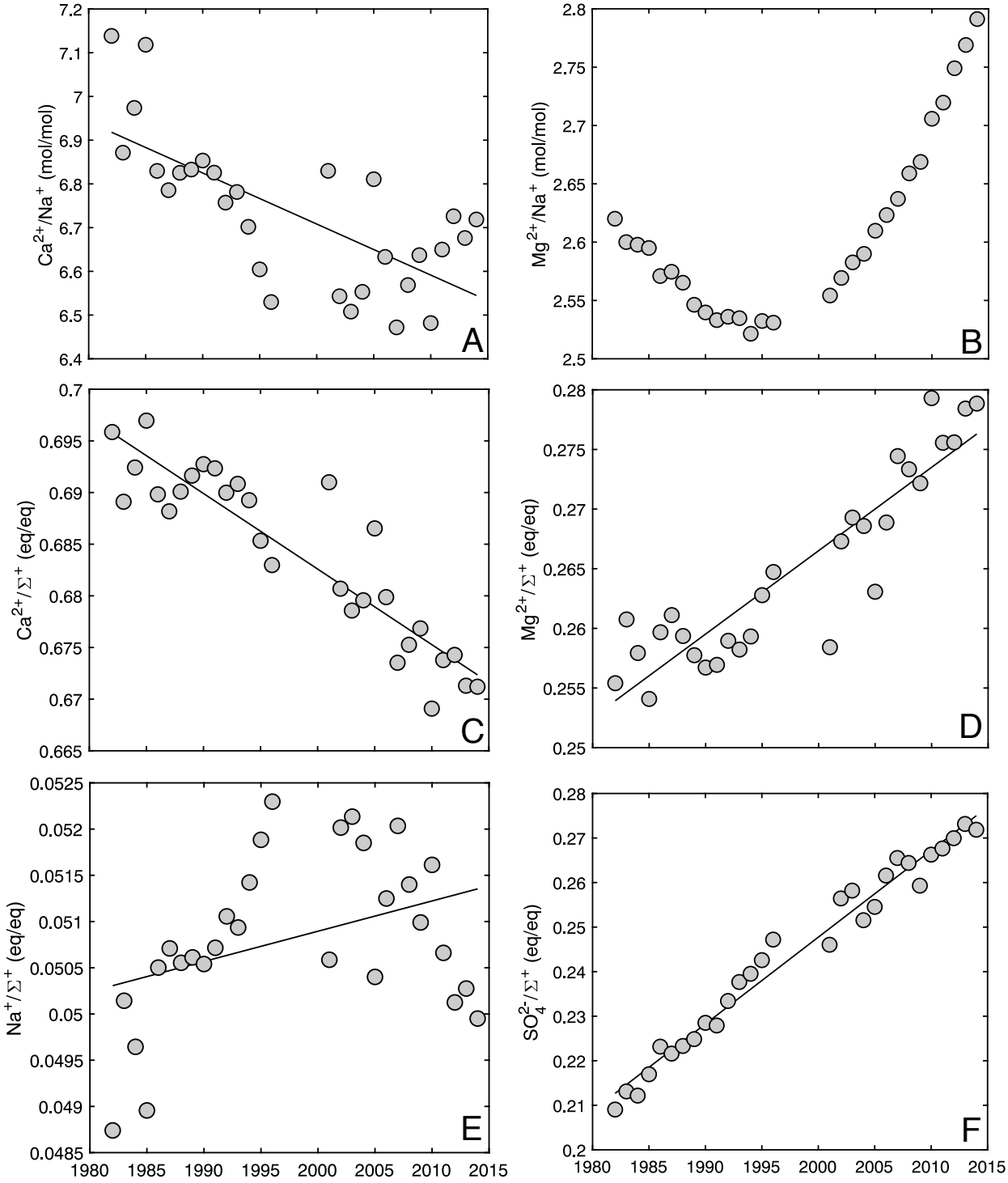

Fig. S19: Multidecadal changes in annual flux ratios for the Yukon River at Pilot (Toohey et al., 2016). (A) Ca^{2+}/Na^{+}, (B) Mg^{2+}/Na^{+}, (C) Ca^{2+}/Σ^{+}, (D) Mg^{2+}/Σ^{+}, (E) Na^{+}/Σ^{+}, and (F) SO_4^{2-}/Σ^{+} between 1982 and 2014. The increase in SO_4^{2-}/Σ^{+} indicates an enhanced role for either sulfide oxidation or evaporite dissolution over the preceding decades. Data were digitized from Toohey et al. (2016).

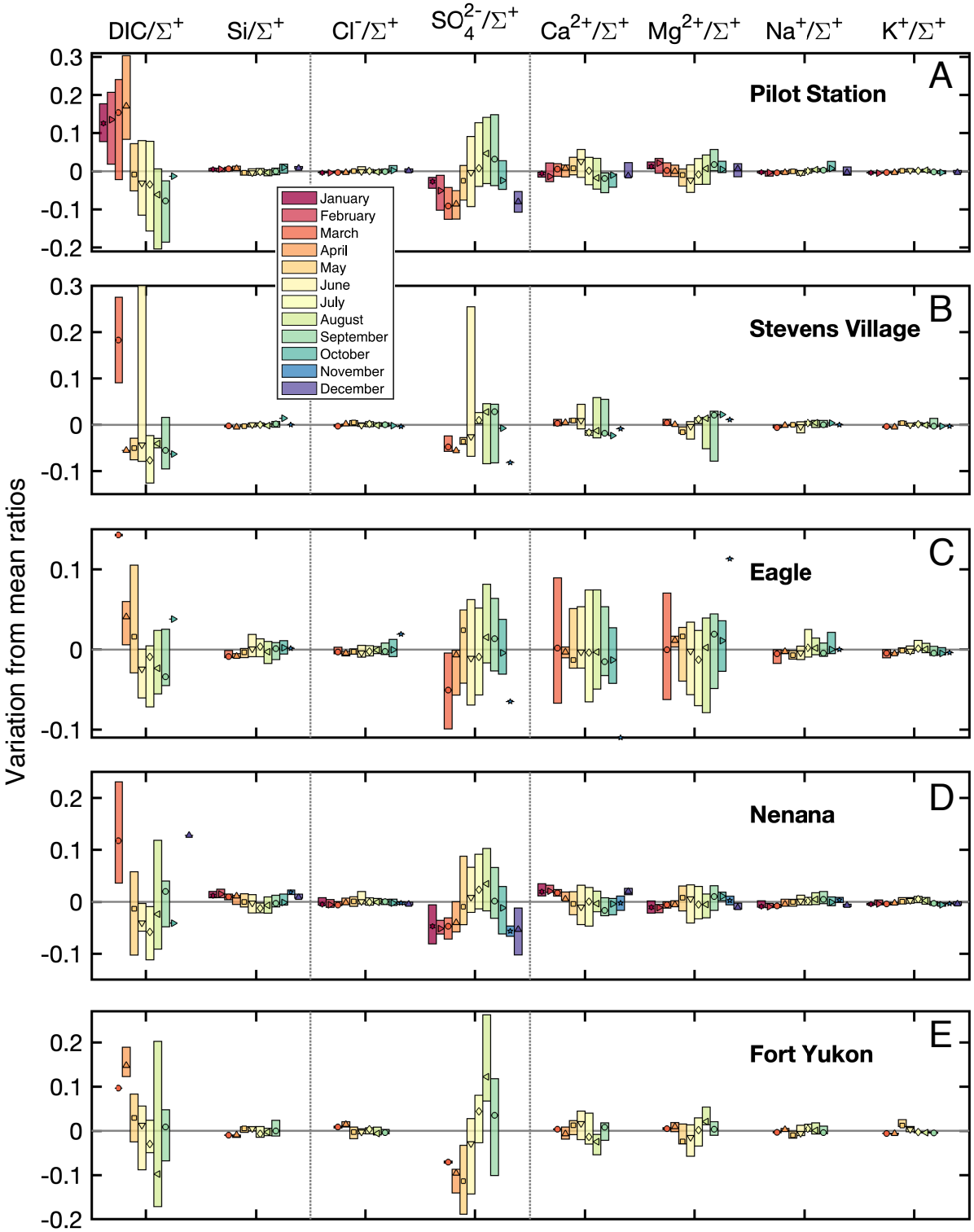

Fig. S20: Summary of timeseries data from the Yukon River Basin. Chemical ratios are shown for each month relative to overall station means for DIC/Σ^+, Si/Σ^+, Cl^-/Σ^+, SO_4^{2-}/Σ^+, Ca^{2+}/Σ^+, Mg^{2+}/Σ^+, Na^+/Σ^+, and K^+/Σ^+ at (A) Pilot Station, (B) Stevens Village, (C) Eagle, (D) Nenana, and (E) Fort Yukon. Colored bars span the 10^{th} to 90^{th} percentile of the variation from the overall mean ratio, and symbols indicate the median variation. Each record is shown in more detail in Figs. S21 - S25.

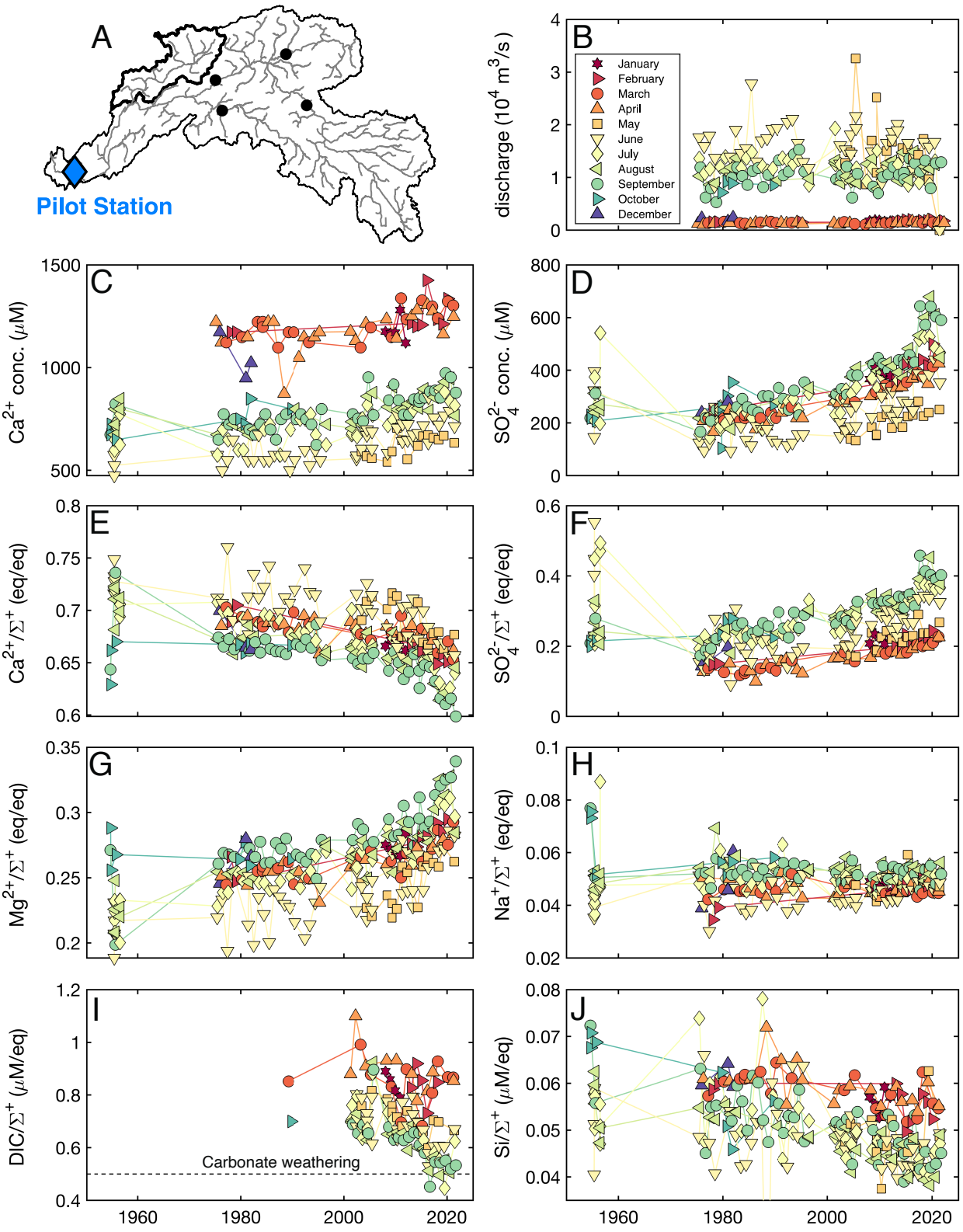

Fig. S21: Timeseries data from the Yukon River at Pilot Station (USGS site number 15565447). (A) Site location, (B) discharge, (C) Ca^{2+} concentration, (D) SO_4^{2-} concentration, (E) Ca^{2+}/Σ^+, (F) SO_4^{2-}/Σ^+, (G) Mg^{2+}/Σ^+, (H) Na^+/Σ^+, (I) DIC/Σ^+, and (J) Si/Σ^+.

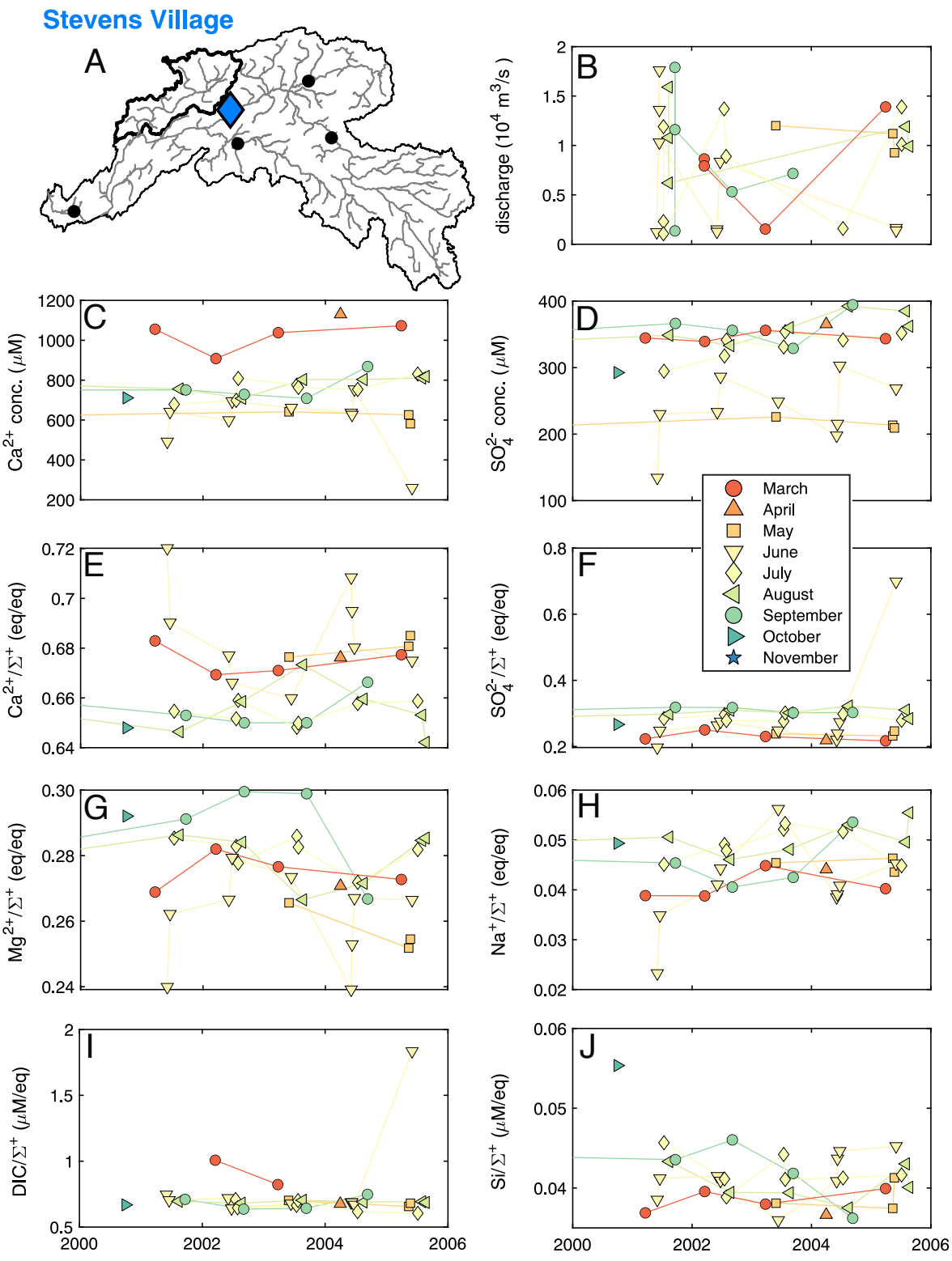

Fig. S22: Timeseries data from the Yukon River at Stevens Village (USGS site number 15453500). (A) Site location, (B) discharge, (C) Ca^{2+} concentration, (D) SO_4^{2-} concentration, (E) Ca^{2+}/Σ^+, (F) SO_4^{2-}/Σ^+, (G) Mg^{2+}/Σ^+, (H) Na^+/Σ^+, (I) DIC/Σ^+, and (J) Si/Σ^+.

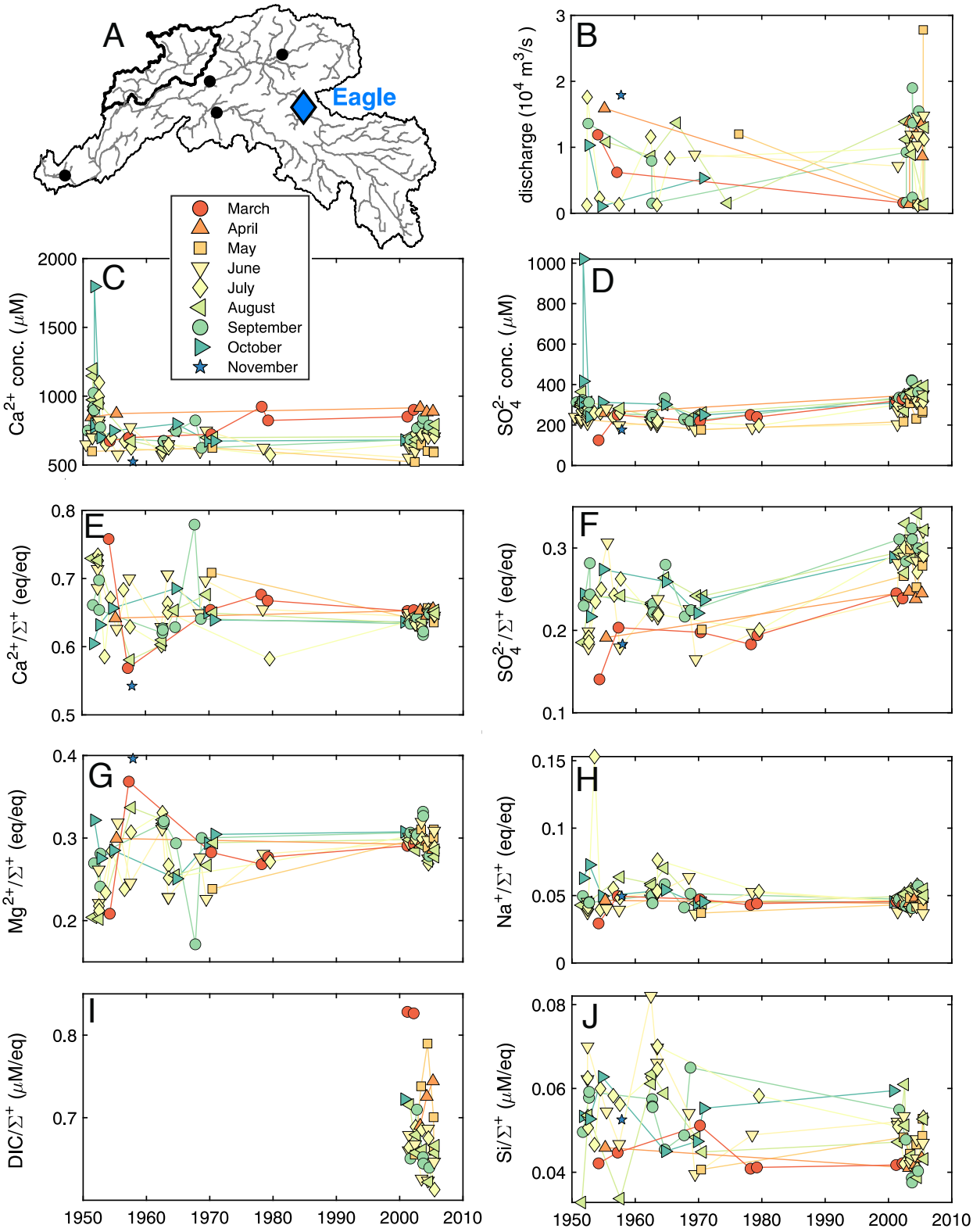

Fig. S23: Timeseries data from the Yukon River at Eagle (USGS site number 15356000). (A) Site location, (B) discharge, (C) Ca^{2+} concentration, (D) SO_4^{2-} concentration, (E) Ca^{2+}/Σ^+, (F) SO_4^{2-}/Σ^+, (G) Mg^{2+}/Σ^+, (H) Na^+/Σ^+, (I) DIC/Σ^+, and (J) Si/Σ^+.

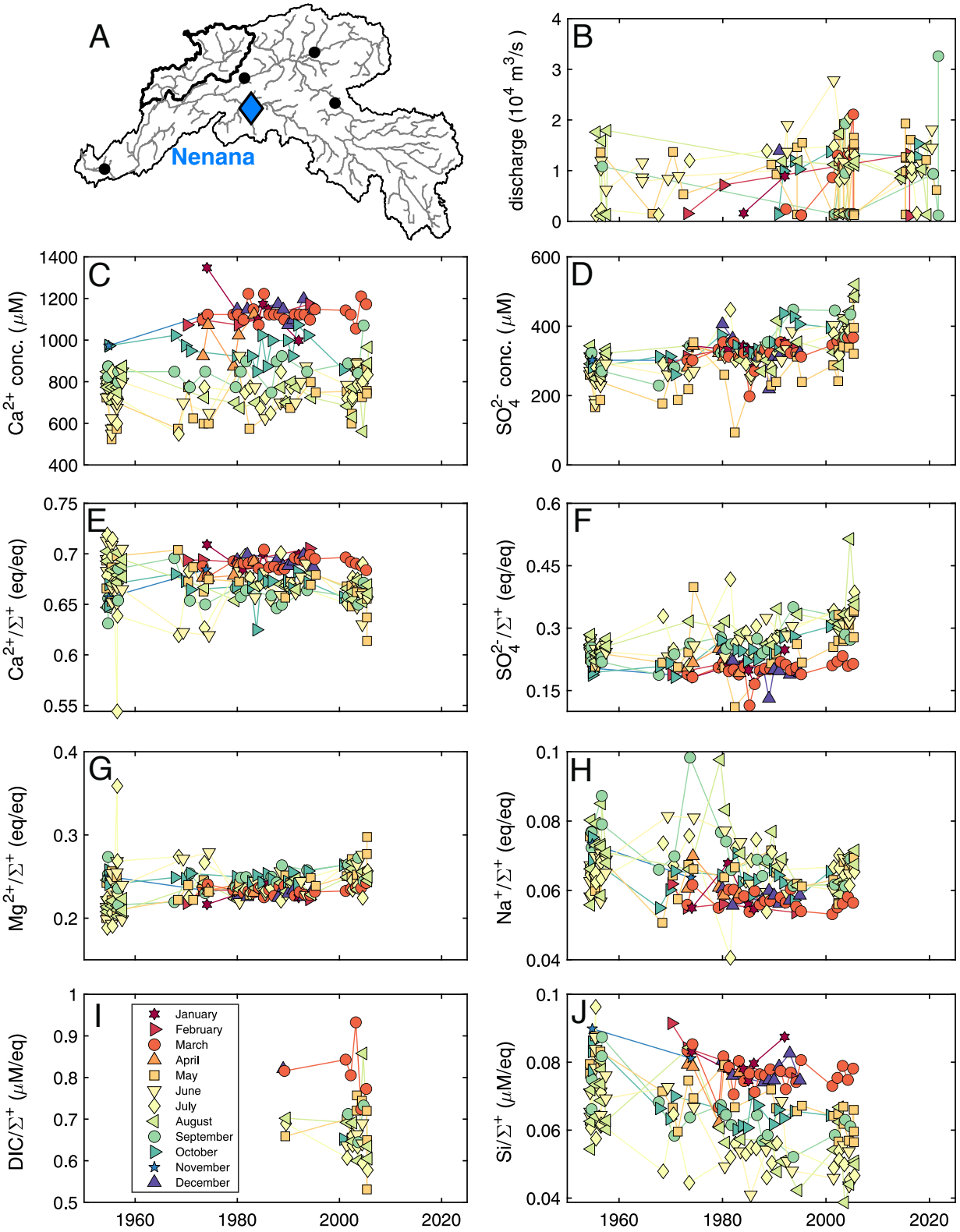

Fig. S24: Timeseries data from the Tanana River at Nenana (USGS site number 15515500). (A) Site location, (B) discharge, (C) Ca^{2+} concentration, (D) SO_4^{2-} concentration, (E) Ca^{2+}/Σ^+, (F) SO_4^{2-}/Σ^+, (G) Mg^{2+}/Σ^+, (H) Na^+/Σ^+, (I) DIC/Σ^+, and (J) Si/Σ^+.

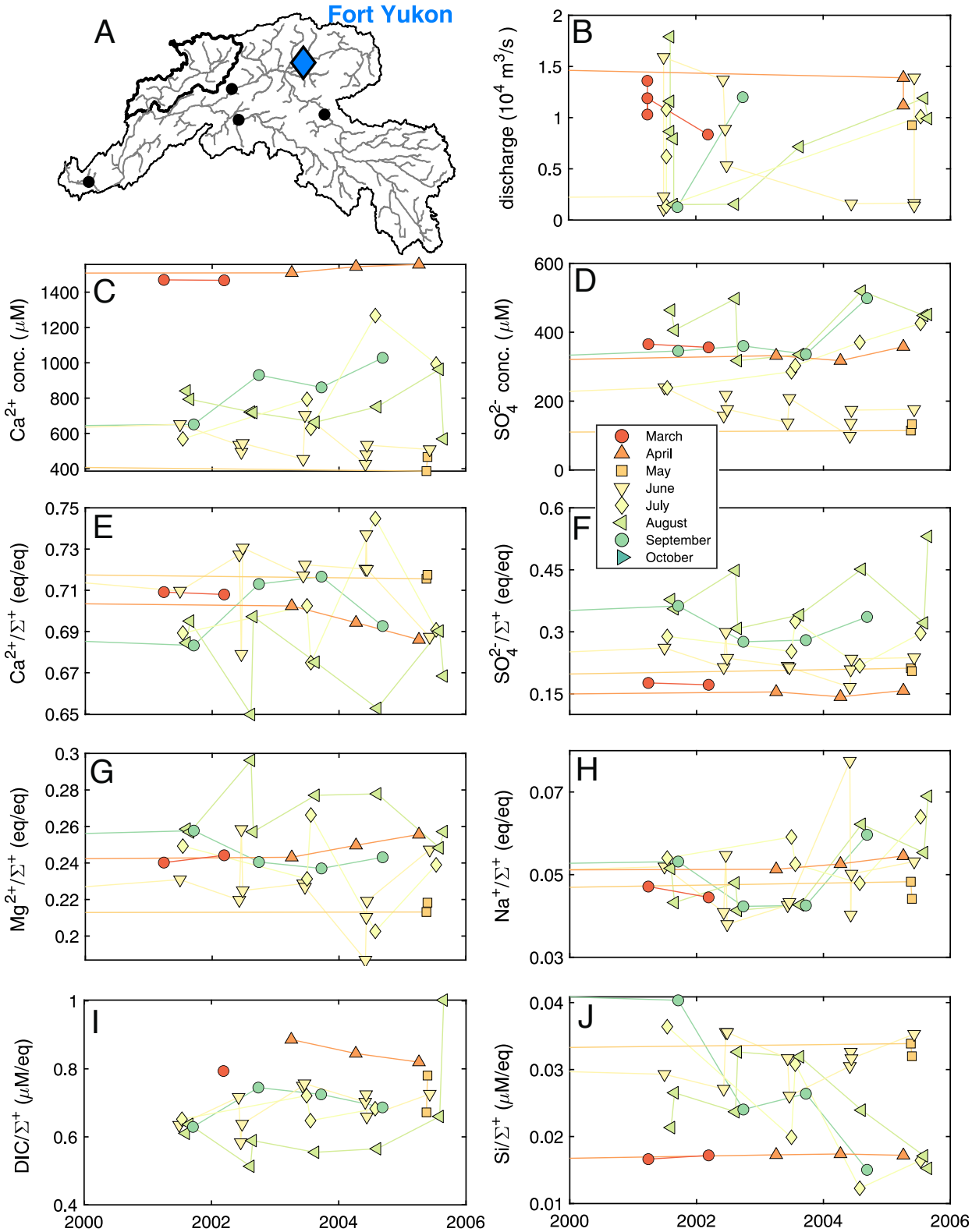

Fig. S25: Timeseries data from the Porcupine River near Fort Yukon (USGS site number 15389000). (A) Site location, (B) discharge, (C) Ca^{2+} concentration, (D) SO_4^{2-} concentration, (E) Ca^{2+}/Σ^+, (F) SO_4^{2-}/Σ^+, (G) Mg^{2+}/Σ^+, (H) Na^+/Σ^+, (I) DIC/Σ^+, and (J) Si/Σ^+.

References

Bataille, C.P., Brennan, S.R., Hartmann, J., Moosdorf, N., Wooller, M.J. and Bowen, G.J., 2014. A geostatistical framework for predicting variations in strontium concentrations and isotope ratios in Alaskan rivers. *Chemical Geology*, 389, pp.1-15. https://doi.org/10.1016/j.chemgeo.2014.08.030.

Barker, A.J., Douglas, T.A., Jacobson, A.D., McClelland, J.W., Ilgen, A.G., Khosh, M.S., Lehn, G.O. and Trainor, T.P., 2014. Late season mobilization of trace metals in two small Alaskan arctic watersheds as a proxy for landscape scale permafrost active layer dynamics. *Chemical Geology*, 381, pp.180-193. https://doi.org/10.1016/j.chemgeo.2014.05.012.

Blum, J.D., Gazis, C.A., Jacobson, A.D. and Page Chamberlain, C., 1998. Carbonate versus silicate weathering in the Raikhot watershed within the High Himalayan Crystalline Series. *Geology*, 26(5), pp.411-414. https://doi.org/10.1130/0091-7613(1998)026<0411:CVSWIT>2.3.CO;2.

Brennan, S.R., Fernandez, D.P., Mackey, G., Cerling, T.E., Bataille, C.P., Bowen, G.J. and Wooller, M.J., 2014. Strontium isotope variation and carbonate versus silicate weathering in rivers from across Alaska: Implications for provenance studies. *Chemical Geology*, 389, pp.167-181. https://doi.org/10.1016/j.chemgeo.2014.08.018.

Cooper, R.J., Wadham, J.L., Tranter, M., Hodgkins, R. and Peters, N.E., 2002. Groundwater hydrochemistry in the active layer of the proglacial zone, Finsterwalderbreen, Svalbard. *Journal of Hydrology*, 269(3-4), pp.208-223. https://doi.org/10.1016/S0022-1694(02)00279-2.

Douglas, T.A., Blum, J.D., Guo, L., Keller, K. and Gleason, J.D., 2013. Hydrogeochemistry of seasonal flow regimes in the Chena River, a subarctic watershed draining discontinuous permafrost in interior Alaska (USA). *Chemical Geology*, 335, pp.48-62. https://doi.org/10.1016/j.chemgeo.2012.10.045.

Douglas, M.M., Li, G.K., Fischer, W.W., Rowland, J.C., Kemeny, P.C., West, A.J., Schwenk, J., Piliouras, A.P., Chadwick, A.J. and Lamb, M.P., 2022. Organic carbon burial by river meandering partially offsets bank erosion carbon fluxes in a discontinuous permafrost floodplain. *Earth Surface Dynamics*, 10(3), pp.421-435. https://doi.org/10.5194/esurf-10-421-2022.

Edmond, J.M., 1992. Himalayan tectonics, weathering processes, and the strontium isotope record in marine limestones. *Science*, 258(5088), pp.1594-1597. https://doi.org/10.1126/science.258.5088.1594.

Gooseff, M.N., McKnight, D.M., Lyons, W.B. and Blum, A.E., 2002. Weathering reactions and hyporheic exchange controls on stream water chemistry in a glacial meltwater stream in the McMurdo Dry Valleys. *Water Resources Research*, 38(12), pp.15-1. https://doi.org/10.1029/2001WR000834.

Kang, M., Skierszkan, E., Brennan, S., Fernandez, D.P., Yang, Z., Girard, I., Gammon, P., de Laplante, G. and Bataille, C.P., 2022. Controls of lithium isotope spatial variability across the Yukon River: Implications for weathering processes in a warming subarctic basin. *Geochimica et Cosmochimica Acta*, 323, pp.1-19. https://doi.org/10.1016/j.gca.2022.02.016.

Keller, K., Blum, J.D. and Kling, G.W., 2007. Geochemistry of soils and streams on surfaces of varying ages in arctic Alaska. *Arctic, Antarctic, and Alpine Research*, 39(1), pp.84-98. https://doi.org/10.1657/1523-0430(2007)39[84:GOSASO]2.0.CO;2.

Keller, K., Blum, J.D. and Kling, G.W., 2010. Stream geochemistry as an indicator of increasing permafrost thaw depth in an arctic watershed. *Chemical Geology*, 273(1-2), pp.76-81. https://doi.org/10.1016/j.chemgeo.2010.02.013.

Kemeny, P.C. and Torres, M.A., 2021. Presentation and applications of mixing elements and dissolved isotopes in rivers (MEANDIR), a customizable MATLAB model for Monte Carlo inversion of dissolved river chemistry. *American Journal of Science*, 321(5), pp.579-642. https://doi.org/10.2475/05.2021.03.

Lehn, G.O., Jacobson, A.D., Douglas, T.A., McClelland, J.W., Barker, A.J. and Khosh, M.S., 2017. Constraining seasonal active layer dynamics and chemical weathering reactions occurring in North Slope Alaskan watersheds with major ion and isotope ($\delta^{34}S_{SO4}$, $\delta^{13}C_{DIC}$, $^{87}Sr/^{86}Sr$, $\delta^{44/40}Ca$, and $\delta^{44/42}Ca$) measurements. *Geochimica et Cosmochimica Acta*, 217, pp.399-420. https://doi.org/10.1016/j.gca.2017.07.042.

Lopez, C.L., Brouchkov, A., Nakayama, H., Takakai, F., Fedorov, A.N. and Fukuda, M., 2007. Epigenetic salt accumulation and water movement in the active layer of central Yakutia in eastern Siberia. *Hydrological Processes: An International Journal*, 21(1), pp.103-109. https://doi.org/10.1002/hyp.6224.

MacLean, R., Oswood, M.W., Irons, J.G. and McDowell, W.H., 1999. The effect of permafrost on stream biogeochemistry: a case study of two streams in the Alaskan (USA) taiga. *Biogeochemistry*, 47(3), pp.239-267. https://doi.org/10.1007/BF00992909.

Maher, K. and Chamberlain, C.P., 2014. Hydrologic regulation of chemical weathering and the geologic carbon cycle. *Science*, 343(6178), pp.1502-1504. https://doi.org/10.1126/science.1250770.

Maher, K. and Druhan, J., 2014. Relationships between the transit time of water and the fluxes of weathered elements through the critical zone. *Procedia Earth and Planetary Science*, 10, pp.16-22. https://doi.org/10.1016/j.proeps.2014.08.004.

Petrone, K.C., Jones, J.B., Hinzman, L.D. and Boone, R.D., 2006. Seasonal export of carbon, nitrogen, and major solutes from Alaskan catchments with discontinuous permafrost. *Journal of Geophysical Research: Biogeosciences*, 111(G2). https://doi.org/10.1029/2005JG000055.

Petrone, K.C., Hinzman, L.D., Shibata, H., Jones, J.B. and Boone, R.D., 2007. The influence of fire and permafrost on sub-arctic stream chemistry during storms. *Hydrological Processes: An International Journal*, 21(4), pp.423-434. https://doi.org/10.1002/hyp.6247.

Rutter, N., Hodson, A., Irvine-Fynn, T. and Solås, M.K., 2011. Hydrology and hydrochemistry of a deglaciating high-Arctic catchment, Svalbard. *Journal of Hydrology*, 410(1-2), pp.39-50. https://doi.org/10.1016/j.jhydrol.2011.09.001.

Shields, G.A. and Mills, B.J., 2021. Evaporite weathering and deposition as a long-term climate forcing mechanism. *Geology*, 49(3), pp.299-303. https://doi.org/10.1130/G48146.1.

Tipper, E.T., Bickle, M.J., Galy, A., West, A.J., Pomiès, C. and Chapman, H.J., 2006. The short term climatic sensitivity of carbonate and silicate weathering fluxes: insight from seasonal variations in river chemistry. *Geochimica et Cosmochimica Acta*, 70(11), pp.2737-2754. https://doi.org/10.1016/j.gca.2006.03.005.

Toohey, R.C., Herman-Mercer, N.M., Schuster, P.F., Mutter, E.A. and Koch, J.C., 2016. Multidecadal increases in the Yukon River Basin of chemical fluxes as indicators of changing flowpaths, groundwater, and permafrost. *Geophysical Research Letters*, 43(23), pp.12-120. https://doi.org/10.1002/2016GL070817.

Torres, M.A., West, A.J. and Li, G., 2014. Sulphide oxidation and carbonate dissolution as a source of CO_2 over geological timescales. *Nature*, 507(7492), pp.346-349. https://doi.org/10.1038/nature13030.

Wadham, J.L., Cooper, R.J., Tranter, M. and Hodgkins, R., 2001. Enhancement of glacial solute fluxes in the proglacial zone of a polythermal glacier. *Journal of Glaciology*, 47(158), pp.378-386. https://doi.org/10.3189/172756501781832188.

West, A.J., Galy, A. and Bickle, M., 2005. Tectonic and climatic controls on silicate weathering. *Earth and Planetary Science Letters*, 235(1-2), pp.211-228. https://doi.org/10.1016/j.epsl.2005.03.020.

White, A.F., Bullen, T.D., Vivit, D.V., Schulz, M.S. and Clow, D.W., 1999. The role of disseminated calcite in the chemical weathering of granitoid rocks. *Geochimica et Cosmochimica Acta*, 63(13-14), pp.1939-1953. https://doi.org/10.1016/S0016-7037(99)00082-4.